A computational study of structural and excitonic properties of chlorosomes

Li, X.

APPENDIX A

Supporting Information for Chapter 2

Relating layer lines to chirality: Fourier-Bessel reconstruction

The usual way of representing a 3D ideal helical/chiral tube assembly[45] is by unrolling it onto a 2D lattice of unit cells spanned by the two independent vectors **a** and **b** at an angle γ, see Figure A.1. Any point A on the lattice can be written as $\mathbf{A} = n_1\mathbf{a} + n_2\mathbf{b}$, in short $A(n_1, n_2)$, and the lattice is fully determined by $a = |\mathbf{a}|$, $b = |\mathbf{b}|$ and γ. For single wall carbon nanotube (SWNT), these lattice parameters follow directly from the atomic honeycomb lattice of graphene,[186] but for chlorosomes they are provided by the optimized unit cell. The chiral vector $\mathbf{C}(n_1, n_2)$ (also rolling or circumferential vector) is to be mapped to the tube circumference, and defines both the chirality and the tube radius R via $|\mathbf{C}| = 2\pi R$, while the translation/axial vector **T** is parallel to the tube axis, $\mathbf{T} \cdot \mathbf{C} = 0$, see Figure A.1.

In the reconstruction method, helices with the same axial translational symmetry, *i.e.* corresponding to sets of parallel lines in the 2D lattice, are assigned to a helical family $H(h, k; n)$, identified by their Miller index (h, k) and the number of crossings $|n|$ with the chiral vector **C**. This n defines the chirality of the family ($n < 0$ for a left-handed helical family) and specifies the order of the Bessel functions J_n that describe the distribution of amplitudes along the associated layer line in reciprocal space. Consequently, the measured distribution provides direct information on the helical family; especially for large tube radii

R, it is dense and skewed towards the meridian. Helices in a family are fully described by their pitch P and the tube radius R, with a chiral angle given by $\delta = \arctan(P/2\pi R)$, while the axial repeat (or repeat distance) $d = P/n$ describes the spacing between adjacent helices. Each helical family $H(h, k; n)$ constitutes one layer line in reciprocal space, and its distance to the equator relates to the reciprocal value of the axial repeat d for that family.

Layer lines thus contain a wealth of information that can be exploited for detailed analysis of chiral structures. Yet, concentrating on chlorosomes of a particular type (WT or mutant), all layer lines derived from experimental structures, obtained by averaging FFT responses over a number of these assemblies, are found to be obscured by a low signal-to-noise ratio, and even the simpler question whether a pure meridian signal is observed cannot be firmly answered. From close visual inspection, one could even be tempted to conclude that the FFT data for mutant chlorosomes lacks a pure meridian signal.[45] Moreover, theoretical analysis for chiral tubular structures shows that the signature of the signal along layer lines is strongly affected by minute ($< 10°$) out-of-plane rotations, which may even produce a pure meridian signal when it is absent for the original (unrotated) case, while the layer line positions are only marginally affected by this rotation. This finding indicates that the signature of the layer line is very sensitive to minute tilts with respect to the plane of imaging that may be introduced in sample preparation prior to cryo-EM,[63] and should lead to the conclusion that any particular signature extracted from the noisy data does not have much value if these conditions are unknown. Concentrating on the layer line position, our challenge boils down to relating the single visible layer line to the proper helical family of the tube.[63,103] Since long-range order is clearly less defined for these systems, the most likely candidates for this basis helical family is when $|h| + |k|$ is minimal, *i.e.* for $H(1, 0)$ or $H(0, 1)$, corresponding to assembly along the **a** or **b** direction, respectively.

Straightforward geometrical analysis of the 2D Bravais lattice provides the axial repeat distances d_a and d_b along these principle directions as a function of the chiral angle δ:

$$d_\mathrm{a} = d_{(1,0)}(\gamma, \delta) = \left|\frac{b \sin\gamma}{\cos\delta}\right|, \delta \neq 90°$$

$$d_\mathrm{b} = d_{(0,1)}(\gamma, \delta) = \left|\frac{a \sin\gamma}{\cos(\gamma - \delta)}\right|, \delta \neq \gamma - 90°$$

with the chiral angle δ between **a** and the chiral vector $\mathbf{C} = (n_2 b \sin\gamma, n_1 a + n_2 b \cos\gamma)^T$ defined as $\cos\delta = (n_1 a + n_2 b \cos\gamma)/|\mathbf{C}|$. The fact that two axial repeat values are relevant reflects the topological transition taking place between rolling along **a** or **b**, at a cross-over angle δ_c defined by $a\cos(\delta_c) = b\cos(\gamma - \delta_c)$. The additional axial repeat distance, d_{armchair}, is provided for completeness, and corresponds to the chlorosome version of the armchair conformation in SWNT, with

$$d_{\text{armchair}} = d_{(1,1)}(\gamma, \delta) = \left|\frac{ab\sin(\gamma)}{\cos(\gamma_1 - \delta)\sqrt{a^2 + b^2 + 2ab\cos(\gamma)}}\right|$$

and γ_1 the (fixed) angle between the $H(1,1)$ direction and **a**.

We note that our expression for the axial repeat along **b**, d_b, does not match the one provided in Günther *et al.*,[45] *i.e.* $d = a\sin\delta$. For completeness, we mention that the different definitions of the chiral angle, our δ and their angle $\delta_{\text{ref}} = 180° - \delta$, are insignificant because of the properties of the sinus.

Variability of the tube radius

The tube radius $R = |\mathbf{C}|/2\pi$ is proportional to the length of the lattice vector $\mathbf{C}(n_1, n_2)$ that defines the rolling direction of the Bravais lattice into a defect-free tubular chiral structure, *i.e.* with (n_1, n_2) mapping to $(0, 0)$. This means that only closed tubes of a commensurate R can be formed, which restricts the number of commensurate chiral angles δ for a fixed R. The NMR finding that local structure in chlorosomes is well defined suggests that the chiral angle δ, which is closely related to the local BChl packing, is roughly equal for different radii in nested tubes. We are interested in analyzing the inverse problem: we want to determine the vector on the lattice, *i.e.* $\mathbf{C}(n_1, n_2)$, and the corresponding tube radius $R = |\mathbf{C}|/2\pi$, associated with the smallest variation $\Delta\delta(n_1)$ around a fixed chiral angle δ_0 for all $n_1 \in \mathbb{N}$. This fixed angle δ_0 is the experimental value determined by geometrical analysis: $\delta_0 = 112.3°$ for BChl *c* and $\delta_0 = 19.8°$ for BChl *d*.

Figure A.4 shows $\Delta\delta(n_1)$ and R for varying $n_1 \in \mathbb{N}$, validating that the distribution of radii R is quite dense in $\mathbb{R}$ when a small deviation in δ (up to about 1 %) is acceptable. The left panel shows the data for $\delta_0 = 112°$ for BChl *c*: values that match the commensurability condition $|\Delta\delta(n_1)| < 0.2°$ are marked by dashed line and relate to the lattice vectors $\mathbf{C}(n_1, n_2) = (4,$

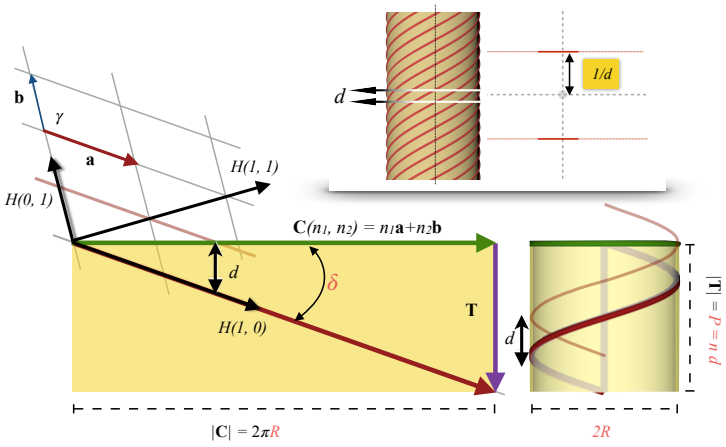

Figure A.1: The 2D Bravais lattice is fully determined by (a, b, γ). In mapping to 3D, the chiral vector $\mathbf{C}(n_1, n_2)$ maps to the tube circumference, providing the tube radius R as $|\mathbf{C}| = 2\pi R$; the translation/axial vector $\mathbf{T}$ maps parallel to the tube axis. The three key helix families $H(1,0)$, $H(0,1)$ and $H(1,1)$, associated with axial repeat distances d_{a}, d_{b} and d_{armchair}, are explicitly shown. The chiral angle δ is defined as the angle between $\mathbf{C}$ and $\mathbf{a}$. The pitch P is defined as the axial advance of a helix after one complete turn. The axial repeat d of the principle helical family relates to the intrinsic repeat distance d of the tube assembly structure along tube axis, which determines the position of the main layer line signal on the diffraction picture. For a n-start helical family, $P = n \cdot d$.

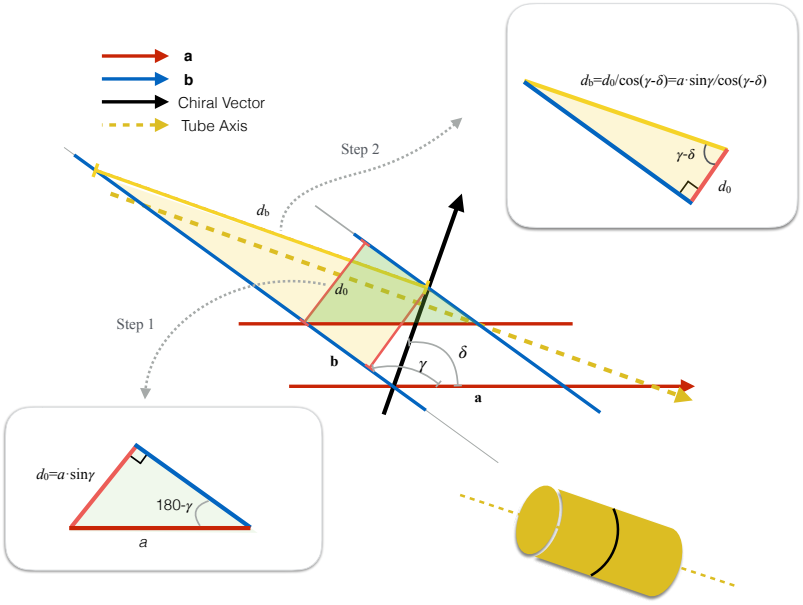

Figure A.2: Geometrical derivation of the axial repeat distance d_b associated with helix family $H(0,1)$.

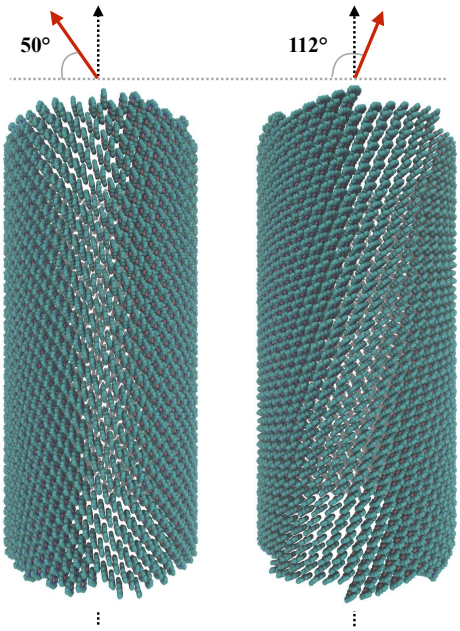

Figure A.3: Snapshots of pre-assembled helical tubes: $\delta = 50°$ (left) and $\delta = 112°$. For clarity, side groups of the head part and tails are not shown. The **a** packing vectors are shown by red arrows.

27), (6, 40), (8, 54), (10, 67), (12, 81), (14, 94), (16, 108) and (18, 121). The corresponding radii $R = 3.8, 5.6, 7.5, 9.3, 11.3, 13.1, 15.1$ and 16.9 nm agree well with the earlier determined experimental values for the *bchR* mutant: $R_{\text{exp}} = 3.7, 5.5, 7.4, 9.2, 11.1, 12.9, 14.7$ and 16.6 nm. The right panel shows data for $\delta_0 = 19°$ for BChl *d*, determined for a slightly different unit cell. In this case, fully commensurate values relate to the lattice vectors $\mathbf{C}(n_1, n_2) = (11, 6)$, (22, 12), (33, 18), (44, 24), (55, 30), (66, 36) and (75, 41). The corresponding radii $R = 2.2, 4.4, 6.6, 8.8, 11.0, 13.2$ and 15.0 are to be compared to experimental values for the *bchQRU* mutant. Estimating these radii by measuring them with a ruler, from the rotationally averaged EM images published in Figure S7 in Ganapathy *et al.*,[37] provides: $R_{\text{exp}} = 2.9, 4.9, 6.8, 8.9, 10.8, 13.1$ and 15.2 nm. We again conclude that there is proper agreement between the calculated commensurate tube radii and the experimentally measured radii.

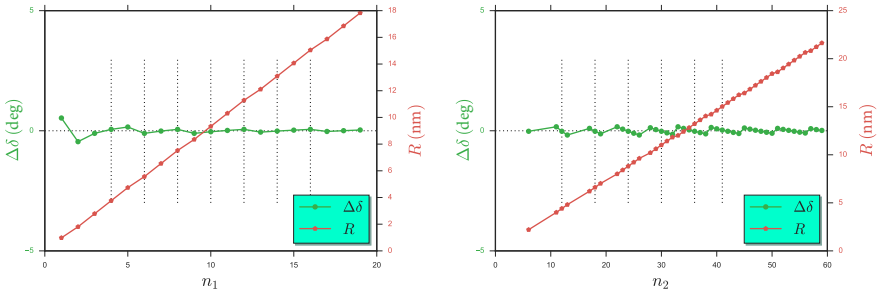

Figure A.4: Radius R of commensurate tubes, associated with chiral vectors $\mathbf{C}(n_1, n_2)$, for which the chiral angle δ is close to the predicted $\delta_0 = 112.3°$ for BChl *c* (left) and $\delta_0 = 19.8°$ for BChl *d* (right). In the calculation for BChl *d*, the different unit cell properties are taken into account. For clarity, only n_1 is shown. For a specific chiral vector (determined by n_1 and n_2), the corresponding deviation $\Delta\delta(n_1)$ from a fixed δ_0 can be found in green on the left vertical axis; the corresponding tube radius R is shown on the right vertical axis (red). Commensurate values, *i.e.* values that satisfying a stringent constraint on the maximum variability of the chiral angle, *i.e.* $|\Delta\delta(n_1)| < 0.2°$, are highlighted by vertical dotted lines.

Determining the layer line position from simulation results

Assemblies obtained by AAMD simulation have been used to generate mimics of electron microscopy (EM) images, by a 2D projection of the electron distri-

bution associated with the atomistic AAMD results. Consequently, just like for experimental EM images, these mimics are passed to a 2D FFT procedure to generate the corresponding power spectra. We employed the EMAN2 software package (http://blake.bcm.edu/emanwiki/EMAN2) that is widely used for single particle reconstruction, helical reconstruction, 2D crystallography and whole-cell tomography, and have set the variable resolution of the calculated electron distribution to 6 Å of experimental EM. Experimentally, tomography would be more appropriate than projection techniques aimed at single particle reconstruction, since the overall shapes of chlorosomal tubes vary substantially, see also the discussion about orientation with respect to the imaging plane in the remainder of this section. Unfortunately, in generating the EM mimic from a simulated AAMD structure, standard EMAN2 disregards contributions due to Mg by not assigning electron distributions for these atom types.

An illustrative EM mimic obtained by standard EMAN2, for a tubular Me-BChl *c* assembly after 1 ns of AAMD simulation at 300 K, as well as its 2D Fourier transform can be found in Figure A.5. The position of the clearly visible layer line signal in Figure A.5 is measured as (1/1.0) nm^{-1}, *i.e.* an axial repeat distance $d = 1.0$ nm close to $|\mathbf{b}| = 0.98$ nm. This agrees well with the theoretical prediction for $\delta = 40°$ and the real space finding that the tube symmetry axis is almost parallel to **b**. For incomplete tubes, like the ones formed by BChl *c* and BChl *d* after 1 ns of AAMD simulation, reduced periodicity gives rise to 2D FFT results with fuzzy and incomplete layer lines, which complicates analysis. An overview of layer line positions extracted from (partial) layer lines for all simulated systems can be found in Table A.3.

We note that estimates for the layer line position can also be extracted directly from the theoretical relation between d and δ, without performing FFT. To illustrate this, we also applied the EMAN2 procedure to a pre-assembled structure consisting of 3 concentric tubes of BChl *c* with $\delta_{1.25} = 112°$. Tubes were built sequentially, *i.e.* by adding BChl *c* molecules one by one to a growing structure, followed by a short constrained AAMD simulation to equilibrate the conformation of the newly added molecule. The stability of the resulting three-tube structure was challenged by another 1 ns of AAMD simulation, and we found that all large-scale structural parameters were conserved. FFT power spectra for this equilibrated structure, obtained via a EMAN2 procedure, are shown in Figure A.6. In particular, the upper left panels show the results of standard EMAN2 (*i.e.* without the Mg contribution, Figure A.6a) and EMAN2

results for Mg only (after replacing Mg by S=Sulphur, an atom that is accounted for in EMAN2, Figure A.6b) based on orthogonal projection.

In experiments, the signal-to-noise ratio is improved by averaging over several spectra calculated for individual chlorosome domains, so we should account for this experimental variability. In particular, when loading chlorosomes to a TEM-grid, individual structures usually experience an (unknown) misalignment or tilt with the grid or imaging plane (and thus with each other) owing to small shape deviations from a perfect tube, in addition to a tiny residual in-plane misalignment after (known) correction for in-plane rotation. For this reason, we introduced a random rotation before projecting the electron distribution to 2D, via `e2project3d -orientgen=eman:delta=2` in EMAN2, and selected six power spectra that closely resemble the spectrum obtained by orthogonal projection. These power spectra, shown in the panels between the upper left and lower right in Figs. A.6a and b, clearly illustrate that a relatively tiny rotation can introduce a diffraction signal on the meridian (meridian signal) without shifting the layer line position. Finally, concentrating on the most distinct signal (stemming from the Mg/S positions, see Figure A.6b), the average over all seven power spectra, shown in the lower right panel, carries a clear layer line signal corresponding to $d = 1.25$ nm, and reproduces several distinct features of the experimental power spectrum.

Details of the computational setup

BChl monomer and *syn-anti* dimer structure

Natural chlorosomes are composed of various BChl homologues that differ in the chemical nature of the side chains R1, R2 and R3 and contain a mixture of R and S stereoisomers at the 3^1 position (Figure A.7a). For BChl *c* R1 = CH3, while for BChl *d* R1 = H. As the main component of natural chlorosomes of *C. tepidum* WT and its *bchQRU* mutant, we simulate the assembly of 17^2-farnesyl-(R or S)-[8-ethyl,12-ethyl]BChl *c* or *d* pigments, which have been considered extensively in the experimental and simulation literature.[37,39,67,100] The ratio between R and S components in the dimer is 1:1 (Figure A.7b) in agreement with Ganapathy *et al.*'s study.[37] A *syn-anti* dimer was identified as the basic

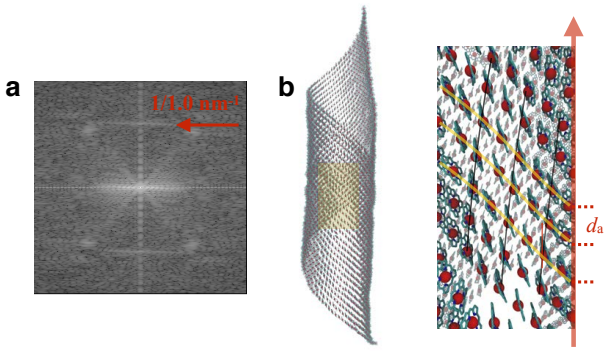

Figure A.5: EM mimic for the closed tubular structure obtained by MD simulation of (40, 30) Me-BChl c system at 300 K after 1 ns, which is shown in Figure 2.3. (a) Power spectrum after 2D Fourier transform. The layer line signal is at $1/d = 1/1.0$ nm^{-1}. (b) Full and zoomed orthogonal projections of real space molecular configuration taken from the final simulation snapshots. Helices along the **a** and **b** direction are highlighted with yellow and black lines, respectively, and the tube axis is shown as a red arrow. The $1/1.0$ nm^{-1} layer line position stems from the axial repeat along the **a** direction, *i.e.* d_a.

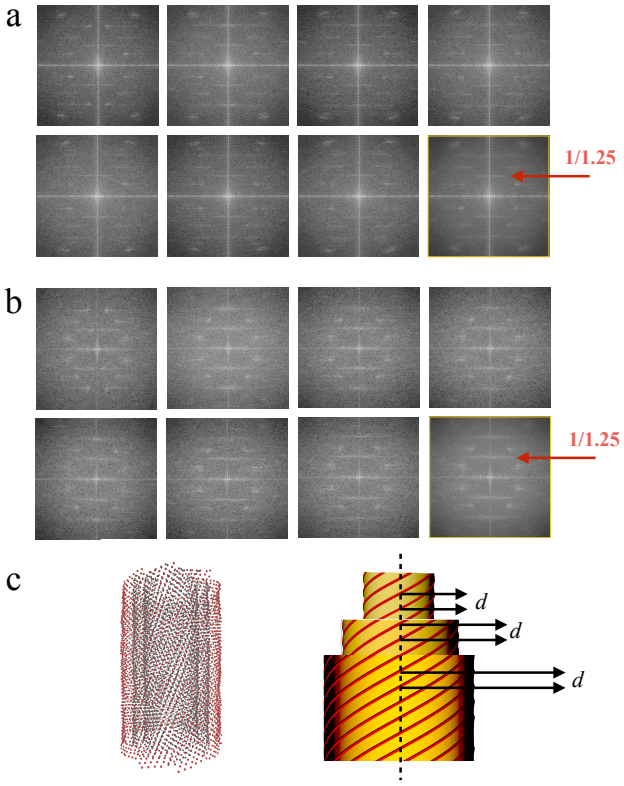

Figure A.6: EM mimics for an equilibrated three-tube BChl *c* structure with $\delta = 112°$: (a) 2D power spectra obtained by the standard EMAN2 procedure that disregards the electron distribution of Mg atoms and (b) 2D power spectra obtained by an EMAN2 procedure that only considers the position of Mg atoms (replacing their electron distribution by that of Sulfur). Different projections were obtained by applying a rotation to the three-tube structure prior to projecting: the upper left result is for an orthogonal projection and lower right the power spectrum after averaging FFT results over all seven considered projections. The layer line signal, labeled by the red arrow, is at $1/d = 1/1.25$ nm^{-1}. (c) Projected snapshot showing the positions of Mg atoms in real space, and schematic image of nested tubes carrying the same chiral angle, illustrating how a distinct layer line line can appear for a multi-tube structure.

structural unit from which the BChl *d* chlorosomes of the *bchQRU* mutant are built, and there is ample evidence that such a unit also plays a key role for other BChl pigments in chlorosomes.[39,118]

The basic motif Mg–O-H$\cdots$O=C for supporting the pigment self-assembly relies on coordination of the magnesium by the 3^1 hydroxyl oxygen functionality of the next BChl within a stack, and hydrogen bonds formed between the hydroxyl hydrogens and the 13 carbonyl oxygens of the BChl in an adjacent stack, see Balaban *et al.*[100] For ease of discussion, we refer to a BChl molecule in terms of a head (ring) and tail (farnesyl) part. When the farnesyl tail is replaced by a methyl group, leaving only a head part, the molecule is denoted as Me-BChl.

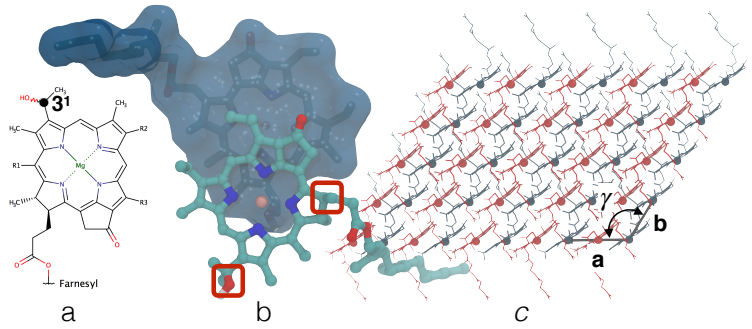

Figure A.7: (a) General structure of BChl molecule. For BChl *c*, R1 = Me, R2 = Et, R3 = Et, while for BChl *d*, R1 = H, R2 = Et, R3 = Me. The hydroxyl group at the 3^1 carbon C atom determines the molecule's chirality, R or S. When the hydroxyl group is at the same side as the wedge bond, the configuration is denoted as *syn*, and *anti* when they are in the opposite directions; (b) The *syn-anti* dimer. Hydrogen bonded with carbon atoms are not shown. The top molecule is in the *syn* configuration with both directions of hydroxyl group and wedge bond out of page (red squares); (c) Initial structure constructed by packing of *syn-anti* dimers in a planar configuration along the principle direction **a** and **b**. This small system is labeled (5, 5); we mainly conducted simulations on a bigger system (30, 30). To distinguish between them, *syn* and *anti* molecules are labeled red and blue respectively, with Mg atoms shown as spheres. Hydrogen atoms are omitted for clarity.

Structure initialization

Since AAMD simulations are generally restricted in terms of attainable time and length scales,[222] the starting structure should be chosen with care to avoid kinetic trapping. Among the models proposed for pigment packing in *bchQRU*, *bchQR* and wild type chlorosomes,[37,39] the *syn-anti* packing model is conserved and we adopt it to prepare our initial structure prior to MD simulation. In particular, our planar starting structure is obtained by prolongating the proposed *syn-anti* dimer structure periodically, using periodicities determined from cryo-EM data: two principle directors **a** and **b**, with length $a = |\mathbf{a}|$ and $b = |\mathbf{b}|$ relating to the experimental repeat distances, at a mutual angle γ (see Figure A.7c). For simplicity, we denote this set of parameters as (a, b, γ). The large scale structure, in terms of the number of periodic repeats of dimers along these two directions, is denoted as (A, B). The structure in Figure A.7c is for (5, 5).

Epimerisation

Chirality at the molecular level can be controlled by cultivation of bacteria under increased photon fluence rates, which in some cases promotes S- over R-epimers at the 3^1-position in BChl *c*.[223] Spectroscopic analysis of reconstructed dye aggregates from these organisms led to the proposition that epimers form separate and individually rather homogeneous rod-like structures, indicative of a different role of R- and S-epimers in photosynthesis. One may thus wonder how handiness affects large-scale curvature formation, particularly since the *syn-anti* dimer employed as a basic structural element in our simulations is a 1:1 mixture of S- and R-epimers.[37] We considered this factor by generating planar assemblies composed of pure S- or R-epimers, noting that our force field does not impose handiness at the 3^1-position via any torsional constraint. Interestingly, we found that the usual $1:1$ ratio of S- and R-epimers is quickly restored after the start of simulation, suggesting that our setup is sufficient for studying tube formation.

MD simulation details

We used the OPLS-AA force field[91,92] in all MD simulations, determined following a protocol developed by Roccatano *et al.*[93] Atomic point charge parameters were obtained by the RESP method[94] at the HF/6-31g* level using Gaussian03 software.[95] Charges obtained at the B3LYP/6-31g* level were also considered and it was found to have little effect on the assembly structure.

MD simulations with periodic boundary conditions along all dimensions were performed with the Gromacs 5.1.2 software package.[96,97] A Particle-mesh Ewald method[98] was used to treat the long-range electrostatic interactions. We performed simulations in a NVT canonical ensemble, maintaining the simulation temperature by a velocity-rescaling thermostat.[99] We perform all simulations *in vacuo* unless otherwise specified. We note that the considered planar starting structure does not reflect natural conditions, since chlorosomes are assembled in a lipid environment which provides the hydrophobic pocket that is needed for kinetic control of the assembly.[224,225] In particular, since BChl pigments are hydrophobic, featureless aggregates will form when pigments are mixed with water. To access this effect on the equilibrium structures obtained by simulation, also a few simulations with organic polar solvents were performed. These simulations were pre-equilibrated using the Berendsen[226] and the Parrinello-Rahman[227,228] barostat.

To accommodate spontaneous curvature formation for the (30, 30) dimer system and to avoid periodicity effects due to boundary conditions, we initially center the planar assembly in a $50 \times 50 \times 50$ nm^3 cubic simulation box. This planar structure was generated using the procedure described earlier, based upon the most recently determined unit cells for BChl *c* and BChl *d*.[37,39] Upon performing an MD simulation, the planar structure for the original set $(a, b, \gamma) = (1.295\ \text{nm}, 0.978\ \text{nm}, 122°)$, with a and b in nm, was found unstable, disintegrating into fragments due to excessive forces at the start of simulation; consequently, all reported simulations start from the parameter set $(1.428\ \text{nm}, 0.987\ \text{nm}, 126°)$, determined from the structure in these stable fragments, instead. For this new set, stable NVT simulations at a reduced temperature of 50 K show a significant decrease of potential energy, within several hundred ps, accompanied by structural rearrangements. A MD trajectory of 1 ns captures global curvature adjustment from the initially planar structure, signaling that the driving force for curving is significant. The resulting stable

structures for 50 K were passed onto simulations for higher temperatures, from 100 K to 300 K (in increments of 50 K). The considered packing parameters, including values extracted from simulation, are summarized in Table A.1.

A 1 ns simulation for a (30, 30) Me-BChl *c* system in vacuum, *i.e.* in the absence of farnesyl tails, confirms that non-bonding interactions between head parts of the pigments are the primary driver for the self-assembly of the dimers to form curved sheets.[118] A long trajectory (50 ns) of a *syn-anti* Me-BChl *c* dimer was also simulated, to reveal their structural stability, and to understand the modulation of this property upon their assembly in a large scale structure.

To assess long simulation time stability of the *syn-anti* packing structure, also a much smaller (5, 5) BChl *c* *syn-anti* dimer system was simulated both in vacuum and in hexane solvents, and the resulting 20 ns NVT trajectories and 10 ns NPT trajectories were analyzed. In addition, a (30, 30) BChl *c* curved structure obtained by simulation in vacuum was used as input for a simulation in hexane, to assess the effect of a commonly used co-solvent on the large scale structural stability.[108]

Table A.1: Summary of packing parameters. The first two sets of packing parameters are used to generate the initial planar structures. The last two sets of packing parameters are determined by analyzing the simulated curved structures of the (30, 30) BChl *c* system at 50 K and 300 K respectively, 1 ns. The distance and angle values are obtained from the coordinates of the Mg atoms from neighboring dimers

	a (nm)	b (nm)	$\gamma(^\circ)$
Initial 1	1.295	0.978	122
Initial 2	1.428	0.987	126
(30, 30) BChl *c* 50 K	1.464 ± 0.027	0.975 ± 0.024	125.1 ± 2.36
(30, 30) BChl *c* 300 K	1.482 ± 0.033	0.980 ± 0.030	124.3 ± 2.87

AIMD simulations

To increase our understanding of the head part dimer assembly behavior, the potential energy for different characteristic structures of the Me-BChl *c* dimer, obtained from MD simulation, were calculated and compared to the energy obtained via Ab-initio molecular dynamics (AIMD) simulations using the Car-

Parrinello Molecular Dynamics (CPMD) package (see http://www.cpmd.org/, Copyright IBM Corp 1990–2019, Copyright MPI für Festkörperforschung Stuttgart 1997–2001.)[229] The PBE exchange-correlation functional was employed and the Kohn-Sham orbitals were expanded in a plane wave basis set with a cut-off energy of 70 Ry. Dispersion-corrected atom-centered pseudopotentials (DCACP) were used for all atomic species.[230] The time-step was set to 4 a.u. The system was evolved at 300 K using a Nose-Hoover thermostat.[231,232]

The reported AIMD simulations were started from the relevant initial geometries imported from AAMD, and simulated for about 600 fs at 300 K. Although the relative angle were found to oscillate around the initial value, their stability was confirmed by AIMD as they remained on average essentially the same. The DFT potential energy initially decreased, because of readjustment of bond distances, and then oscillated around an average value that is reported in Table 2.1 alongside the AAMD values.

Structure properties in curved structure

Large-scale properties of simulated assemblies

Analysis of the simulated tubular structures is complicated by deviations from the ideal case of a Bravais lattice of unit cells mapped to a perfect cylinder. Yet, our simulation snapshots show that these deviations are fairly limited, which is further quantified by application of a least-squares fitting procedure (LSGE, http://www.eurometros.org) to find the corresponding cylinder based on the position of the Mg atoms. Table A.2 shows the radii R of the best fit and standard deviations of the residuals (σ_{res}) for all considered temperatures. This analysis shows that the curved structures obtained after 1 ns of unconstrained AAMD can be sufficiently described by an ideal cylindrical tube for the BChl *c* system considered here. Ideal helical tubular structures are fully quantified by two of the three geometrical parameters defined in the previous section, which are, apart from the tube radius R, two parameters relating to the helical arrangement of pigments: the pitch P, *i.e.* the axial advance of a helix after one complete turn, and the chiral angle δ, *i.e.* the angle between the pitch (a vector with this length along the cylinder symmetry axis) and the plane

of rotation (see Figure 2.4). Such a classification is very common for helical biological structures.[63] Since the third parameter can be directly related to the other two via $\delta = \arctan(P/2\pi R)$, we focus on the pitch P, which we determine directly from the simulated structures to avoid ambiguities that may arise when projecting a 3D structure to a 2D (curved) plane.

In agreement with the standard practice in the analysis of helical structures, and also because our aggregates do not feature complete helical turns, the pitch is determined from local properties: the rotational increment ϵ between two neighboring units (here: adjacent Mg atoms along the **a** direction) and the helical rise h, see Table A.2 for their expectation values and standard deviations. Consequently, the pitch is provided by the relation $P = m \cdot h$, with m the (average) number of Mg atoms (equivalent to the number of pigments) in a complete helical turn, *i.e.* $m = 360°/\epsilon$. From this relation, the standard deviation of the pitch P can be formally estimated as

$$\sigma_P = \frac{360°}{\bar{\epsilon}} \sqrt{\bar{h}^2 \left(\frac{\sigma_\epsilon}{\bar{\epsilon}}\right)^2 + \sigma_h^2} \tag{A.1}$$

if we suppose that there are no covariances between the extracted ϵ and h. Comparing the mean value for the pitch at $T = 50$ K, *i.e.* $\bar{P} = \bar{m} \cdot \bar{h} = 28.8$ nm, to the estimated standard deviation $\sigma_P = 3.9$ nm via Eq. (A.1) suggests that there is a considerable variability in the large-scale structural properties of simulated helical assemblies, even at the lowest temperature considered. Yet, this suggestion is inconsistent with direct visual analysis, which shows a very regular structure.

To further study this issue, we have performed analysis at a much longer length scale and determined the mean chiral angle from values that were calculated for the 30 large (partial) helices constituting the aggregate after 1 ns at $T = 50$ K. This alternative method provides $\bar{\delta} = 26.55°$ and a very modest $\sigma_\delta = 0.38$. Since this $\bar{\delta}$ is fully consistent with the chiral angle $\delta = \arctan(\bar{c}/2\pi R) = 26.55°$ calculated from (mean) local properties, we conclude that the variable local structure indeed does not translate into an equivalent variation of structural properties at the relevant length scales. Apparently, in a stable aggregate, local variations average out. For this reason, we have omitted error bars in Figure 2.4 and focused on the fitted R and mean chiral properties determined from local structure: $\bar{c}$ and $\delta = \arctan(\bar{c}/2\pi R)$.

Table A.2: Local structural data extracted from the simulated curved structures of the (30, 30) BChl *c* at different temperatures.

T	$\bar{\epsilon}$ (degrees)	σ_ϵ (degrees)	$\bar{h}$ (nm)	σ_h (nm)	R (nm)	σ_{res} (nm)
50	3.99	0.20	0.32	0.04	9.3	0.31
100	4.44	0.23	0.38	0.04	8.1	0.28
150	4.93	0.33	0.38	0.04	7.3	0.35
200	5.06	0.43	0.39	0.04	7.0	0.46
250	5.29	0.39	0.37	0.05	6.9	0.31
300	5.32	0.47	0.37	0.05	6.8	0.38

One nanosecond simulation snapshots of initially planar system that are entirely composed of BChl *d* are shown in Figure A.8, for different temperatures T (T = 50, 100, 200 and 300 K). The same procedures as before were applied to extract structural properties of the chiral tube for T = 50 K and yielded the following values: $(a, b, \gamma) = (1.4561 \pm 0.042\ \text{nm}, 0.926 \pm 0.030\ \text{nm}, 122.5 \pm 3.42^\circ)$; fitted radius R = 10.6 nm; mean pitch $\bar{P}$ = 23.0 nm; chiral angle δ = 19.1°.

Mean values of the induced molecular dipole moment

In practice, it is far from straightforward to calculate the direction of the induced molecular dipole moment of a BChl pigment by quantum simulation, since it will be affected by its structured surroundings. This renders the determination of a mean angle between the induced molecular dipole moment and the symmetry axis of the cylinder an intractable task. However, as the orientation of the ring in the head part of the pigment provides an easy computable and useful estimate of this property, we have instead extracted the instantaneous (1 ns snapshot) mean angle β' of the plane formed by the four nitrogens with the cylinder symmetry axis for the different BChls considered in this study (T = 300 K). The results of this exercise are summarized in Table A.3. Since β' is sensitive to out-of-plane macrocycle distortions that are known to affect the planarity of the BChl ring on a short time scale, standard deviations are not reported. Instead, we compare the β' extracted from simulation to the values predicted by the expression introduced in a recent spectroscopic study, which are derived from the unit cell by geometrical considerations.[45] Figure A.9 shows the predicted β' versus the chiral angle δ in the relevant δ-range.

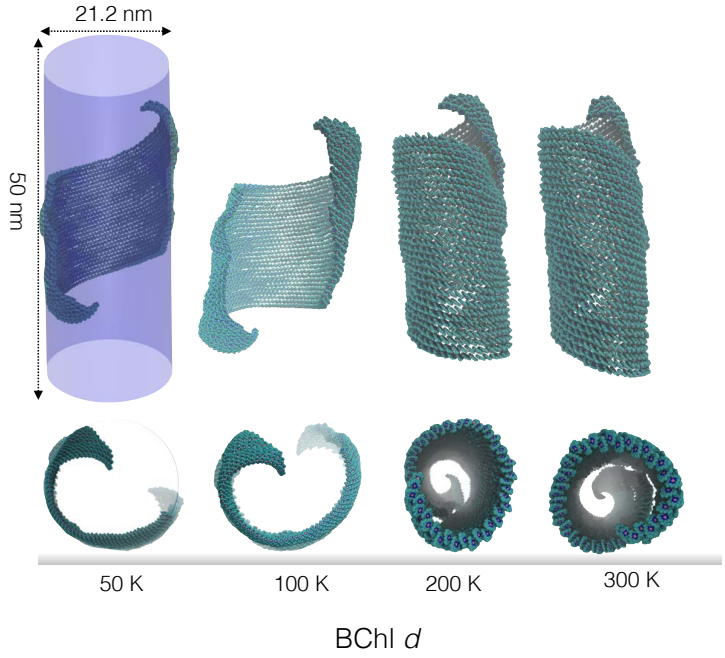

Figure A.8: Simulation results obtained for (30, 30) BChl *d* at 50 K, 100 K, 200 K and 300 K, after 1 ns simulation. For clarity, side groups of the head part and tails are omitted.

The predicted (extracted) values are for the three BChls are (all in degrees): 41 (39) for BChl *d*, 29 (29) for BChl *c* and 19 (18) for Me-BChl *c*, respectively. We conclude that the results of both types of analysis are consistent. A summary of all large-scale chiral tube properties extracted by fitting and *in situ* analysis is presented in Table A.3.

Table A.3: Summary of extracted chiral tube properties for (30, 30) BChl *d* at 50 K, (30, 30) BChl *c* at 300 K and (40, 30) Me-BChl *c* 300 K systems. Snapshots of simulated structures of these systems are shown in Figure 2.3 and Figure A.8. The predicted chiral angles δ based on geometrical analysis of ideal tubes for *bchQRU* ($d = 0.83$ nm) and WT/*bchR* chlorosome ($d = 1.25$ nm) for the relevant unit cell parameters are added in parentheses. $1/d$ determines the layer line position of a simulated EM image. *Since the structures for BChl *c* and *d* are only partial tubes, these values are only estimates.

	(30, 30) BChl *d* 50 K	(30, 30) BChl *c* 300 K	(40, 30) Me-BChl *c* 300 K
R (nm)	10.6	6.8	6.1
δ (deg)	19.1 (19.8)	30.5 (112.3)	40.6
β' (deg)	39.1	29.1	18.2
d(nm)	0.87*	0.95*	1.0

Large-scale tail conformations

We analyzed tail conformations in the curved (30, 30) BChl *c* systems after 1 ns by projecting the 3D curved structure to 2D along the long axis of the fitted cylinder. Using the 2D projection, we determined the radial position, *i.e.* the distance L to the center O of the circle, for a few reference atoms in each of the BChl molecules — Mg, C_1 and C_2 — see Figure A.10c. The end-to-end distance (EED) of the tail part is consequently computed as the difference in the radial position of C_1 and C_2, *i.e.* $L_{OC_1} - L_{OC_2}$, while the (radial) thickness of the layer formed by the tail is computed as the difference in radial position of Mg and C_2 ($L_{OMg} - L_{OC_2}$). The particular range in the EED distribution for $T = 50$ K can be explained in terms of tail conformations that point towards the center of the cylinder (EED > 0), that are parallel to the cylinder axis (EED $= 0$) or directed away from the center, towards neighboring head groups (EED < 0). We find that the distribution of the radial thickness can be fitted by a Gaussian, and we used the peak value plus half the radius of the C_2 carbon $\bar{L}$ to estimate the inter-layer distance $d = 2\bar{L}$ between nested cylinders, assuming that there is

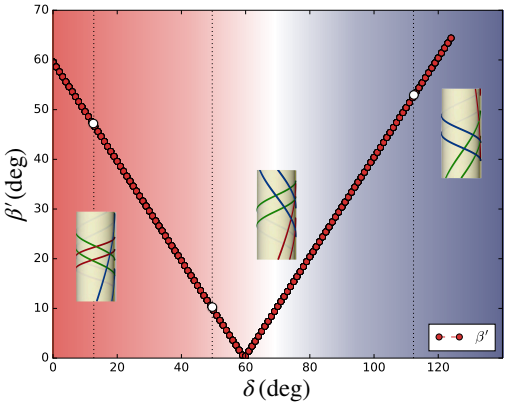

Figure A.9: Predicted β' angles of tubes formed by chiral angles δ between 0° and γ, based on the expression $\beta' = |\delta\text{-}90{+}\eta|$ taken from Günther *et al.*[45] This figure is complementary to Figure 2.2 in the main text. To evaluate this expression, we took $\eta = 30.4°$, which is consistent with the unit cell parameter (1.48 nm, 0.98 nm, 124.3°) used in the Figure 2.2 axial repeat d prediction.

no inter-digitation of tails belonging to BChl molecules in different tubes. The comparison of the estimate d to the consistently found experimental interlayer distance $d_{\text{exp}} = 2.1$ nm, determined from the Bijvoet pair, see Figure A.11, shows that $d \rightarrow d_{\text{exp}}$ with increasing T. We note that the monotonic decrease of d with rising T can also be explained in terms of improved sampling, albeit that the thickness slightly increases for $T = 300$ K. Our finding suggest that there is indeed little or no inter-digitation between tails belonging to neighboring tubes.

Large-scale transition of a planar to a curved aggregate

Details of the transition are shown in Figure A.12, which focuses on the evolution of the total potential energy E (in kJ/mol) with time as well as the stable curved aggregate obtained after 1 ns of simulation (both for $T = 50$ K). The plot of $E - E_0$, *i.e.* E relative to its initial value E_0, shows a steep decrease that is accompanied by the rapid formation of large-scale curvature (see inset of snapshots along the trajectory). Although the curved structure

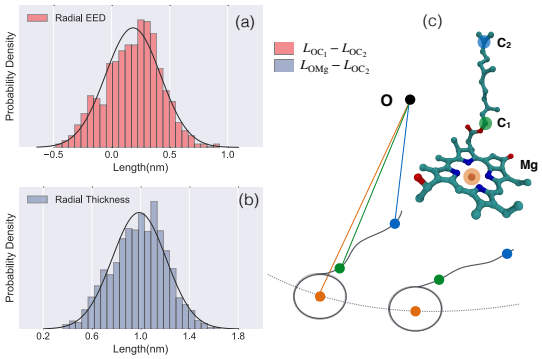

Figure A.10: Spatial analysis of tail configurations in the curved structure, obtained in (30, 30) BChl *c* system at 50 K after 1 ns, projected on fitted cylinder cross-section surface. (a) Distribution of radial end-to-end distance (EED) of tails; (b) Distribution of radial thickness of a single layer pigment molecules; (c) Illustration of how the radial EED ($L_{OC_1} - L_{OC_2}$) and radial thickness ($L_{OMg} - L_{OC_2}$) are determined. O denotes the projected center of the fitted cylinder.

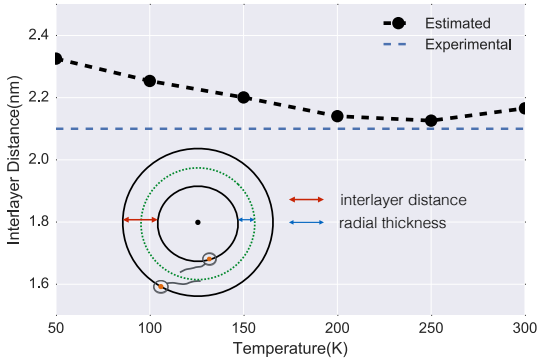

Figure A.11: Inter-layer distances for nested cylinders, as determined from the spatial extent of tails for the simulated curved structures (single cylinder) at different temperatures, from 50 to 300 K (see inset). The inter-layer distances are calculated as two times the radial thickness of a single layer plus one carbon atom van der Waals radius. The experimental inter-layer distance is 2.1 nm.

does not visually change during the last 500 ps of simulation, a non-vanishing driving force for continued curving may be observed from a tiny gradient $\partial E/\partial t$ towards the end of simulation. We note that for a higher temperature, $T = 300$ K, the planar-to-tube transition takes roughly 2 ns. For $T = 50$ K, the curved structure is a very regular on the intermediate scale, with the Mg atoms in the BChl molecules (left side of Figure A.12b; obtained by orthogonal projection of the Mg content in the partial tube) forming a regular lattice. This can be seen from the well-defined layer lines in the power spectrum at the right side of the panel, which shows the 2D Fourier transform of the snapshot at the left.

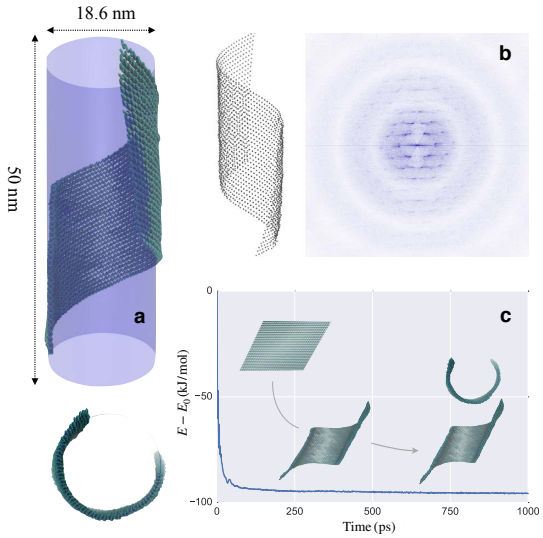

Figure A.12: Simulation results for the (30, 30) BChl *c* system at 50 K: (a) Stable curved structure after 1 ns of simulation and corresponding cylinder, fitted to the Mg atom coordinates using a least-square fitting algorithm (LSGE, http://www.eurometros.org/). For clarity, side groups of the head part and tails are not shown; (b) Mg atom configuration snapshot and corresponding scattering pattern, indicative of a helical structure; (c) Evolution of potential energy E along the trajectory, showing the drop in potential energy that accompanies curving. The initial potential energy E_0 is used as a reference value.

Dynamics of the hydrogen bonded network

Each BChl molecule contains two groups that are capable of forming hydrogen bonds: a Donor (hydroxyl group oxygen) and an Acceptor (carbonyl group oxygen). In order to analyze general properties of the hydrogen bonded network, structures should be sufficiently large to rule out strong effects of the BChl molecules at the boundary, which are naturally restricted in candidates for Donor-Acceptor interactions. Figure A.13 shows the evolution of the total number of established hydrogen bonds in large (30, 30) BChl *c* and BChl *d* assemblies during a 1 ns simulation trajectory. Both systems were simulated at 50 K. A geometric criterion implemented in the Gromacs software (default values) was used to determine whether a hydrogen bond is established and to determine their total number within one structure.

Since the Donor/Acceptor groups are shared by BChl *c* and *d* molecules, the maximum number of hydrogen bonds is 1709 for both cases. From Figure A.13, we see that the number of hydrogen bonds in the assembly structure increases quickly from the (planar) start and saturates to a constant value. This saturation value is around 1190 for BChl *c* and 1517 for BChl *d*. In relative terms, we thus find that 70% of the available hydrogen bonds are established for BChl *c* and 90% for BChl *d*.

In situ analysis: time-dependent sampling distribution of head-head stacking angle α

In addition to the instantaneous sampling distribution of the intra- and inter-dimer angle α shown in Figure 2.7, for the (30, 30) BChl *c* system at 1 ns, we also considered the time-dependent sampling distribution for the part of the trajectory where the structure does not visually change, *i.e.* between 500–1000 ps (in steps of 10 ps) for $T = 50$ K. One of the objectives was to evaluate the role of rotations in the dynamics of the structure; the other to see whether there the sampling distributions for α_{inter} and α_{intra} show evidence for a preferred angle and (possibly) symmetry breaking. The result of this exercise can be found in Figure A.14. The multi-modal nature of the distribution confirms that a small number of configurations are preferentially sampled during the 500 ps trajectory. Since this sampling is obtained for $T = 50$ K and a relatively short trajectory, it shows that the underlying potential energy landscape is rather

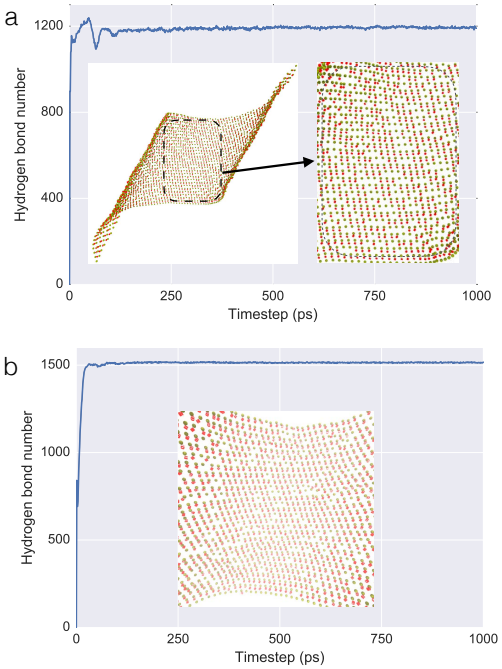

Figure A.13: Evolution of number of hydrogen bonds along the MD simulation trajectory for (a): (30, 30) BChl *c* and (b): (30, 30) BChl *d* system at 50 K. The insets show local details of the hydrogen bonded network in part of the stable curved structures after 1 ns simulation. Green circles indicate Mg atoms; established hydrogen bond are identified by red circles.

flat with rotations taking place on a relatively short time scale. This result, however, does not allow us to draw conclusions about symmetry breaking and the origin of large-scale curvature.

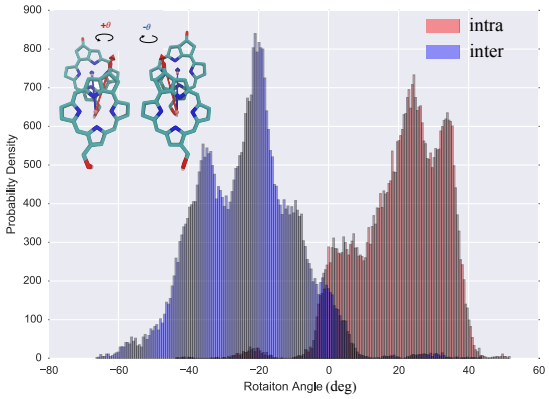

Figure A.14: Distribution of rotation angle α, extracted from the curved structures obtained along trajectory of MD simulation of (30, 30) BChl *c* system at 50 K, from 500 ps to 1 ns.

In situ analysis: sampling distribution of $\Delta\beta$ for a higher temperature

In addition to the relative intra- and inter-molecular rotations α, we also considered a simplified representation that includes handedness. The time-dependent sampling distribution of $\Delta\beta$ for the lowest temperature ($T = 50$ K) considered, see Figure 2.8, sampled between 500–1000 ps (in steps of 5 ps), has a bimodal nature. Although it is clearly skewed towards positive values of $\Delta\beta$, large-scale curvature should result from a pertinent offset in $\Delta\beta$ compared to the fully symmetric case, *i.e.* $\bar{\Delta\beta} = 0°$. For this reason, we additionally evaluated the sampling distribution of $\Delta\beta$ for the highest considered temperature $T = 300$ K using the same procedure, see Figure A.15. We find that the sampling distribution for this higher temperature has a distinct Gaussian shape with a peak position that is small and positive $\bar{\Delta\beta} = 4.6°$. This finding quantifies the symmetry breaking at a local structural level, and clearly identifies the

molecular origin of pertinent curvature at a larger scale.

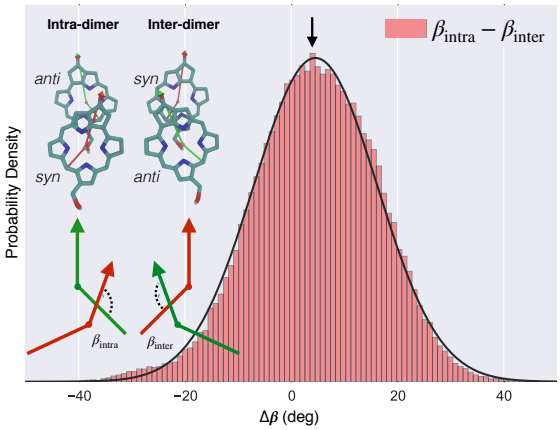

Figure A.15: Distribution of packing angle difference ($\beta_{intra} - \beta_{inter}$) between neighboring intra-dimer and inter-dimer rotation angles, extracted from the curved structures in the trajectory obtained in MD simulation of (30, 30) BChl *c* system at 300 K, from 500 ps to 1 ns. The distribution peaks at 4.6°.

In situ analysis: correlating relative rotation and hydrogen bonding

As can already be anticipated from the starting planar configuration in Figure A.7c, out-of-plane rotation of individual BChl molecules, relative to their neighbors, will affect the network of hydrogen bonded interactions along the **b** direction that plays a role in facilitating the structural integrity of the assembly upon curving, see the discussion about stabilizing interactions in the Chapter 2. To quantify how rotation and hydrogen bonding are related, we considered the relative rotational angle $|\alpha|$ for bonded and non-bonded BChl molecules separately, see Figure A.16.

We adopted standard geometric criteria (Donor-Acceptor distance smaller than 0.35 nm and Hydrogen-Donor-Acceptor angle smaller that 30°), as implemented in Gromacs software package, to determine whether a hydrogen bond is formed. The Donor (carbonyl group oxygen) hydrogen bonding situation is used to determine whether a specific site (molecule) is hydrogen bonded.

Then, its absolute relative rotation angle $|\alpha|$ is determined from the angle with the molecule whose hydroxyl oxygen atom is in close contact with its Mg atom, as the pair structure shown in Figure2.7a (the top molecule is our target molecule for hydrogen bonding state rotation angle analysis). Figure A.16 shows that large relative rotation as expected correlates with the breakage of hydrogen bonds. Yet, the data also confirm that part of the relative rotations are correlated, and that for these cases hydrogen bonds are maintained.

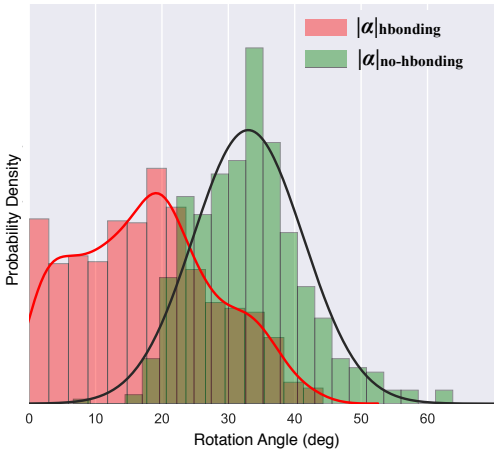

Figure A.16: Relative rotation angle distribution of hydrogen bonded molecules $|\alpha|_{\text{hbonding}}$ and not hydrogen-bonded molecules $|\alpha|_{\text{no-hbonding}}$ for (30, 30) BChl c system at 50 K after 1 ns, see Figure 2.7 and 2.9.

Spectral analysis of rotational degree of freedom

To clarify the spectral properties of a particular (local) vibration, *i.e.* the relative rotation between two molecules in a dimer, which is linked to the formation and breakage of hydrogen bonds, we performed spectral analysis on the time traces of the relative angle α for a few selected dimers. These traces were extracted from a densely sampled (Δt = 10 fs) 25 ps trajectory of the (30, 30) BChl *c* system at 300 K. Since the instantaneous state of a (*syn* or *anti*) monomer in a dimer is either “0-hb”, “1-hb” or “2-hb”, we selected dimers that differ in the number of hydrogen bonds (between 0 to 4) formed between

monomers and their neighbors after 25 ps of simulation. In this analysis, we disregarded whether a hydrogen bond was formed by a molecule in the (*syn* or *anti*) state and also did not explicitly account for changes in the dimeric state along the trajectory.

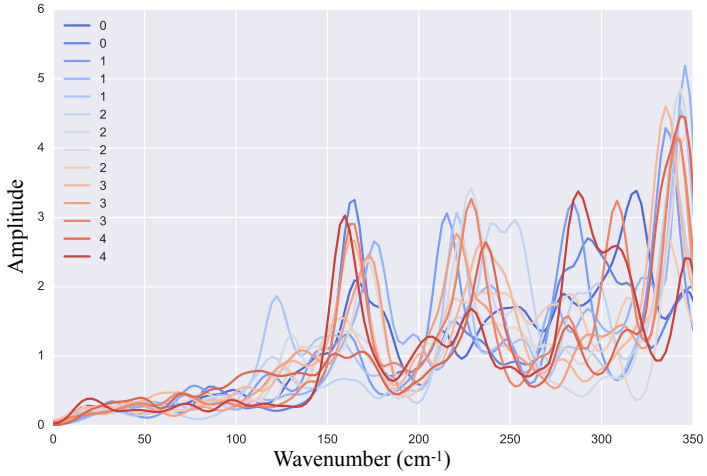

Figure A.17: Fourier spectra (amplitude versus wavenumber) calculated from the time traces of the relative rotational angle α for 14 dimers selected from the large BChl *c* aggregate. The selection criterion was based on a proper representation of the different domains determined by analysis of hydrogen bonding, which is based on individual molecules. Labels indicate the total number of hydrogen bonds formed by the two molecules in the dimers and surrounding molecules at 25 ps.

We considered the effect of a varying number of hydrogen bonds on this spectral analysis by considering a single trace that exhibits a clear change along its short (25 ps) trajectory. We explicitly accounted for this change by performing spectral analysis for the associated partial traces. Although there is an observable difference in the spectra, the position of the first band undergoes only a slightly shift when compared, from around 160 cm^{-1} to 140 cm^{-1}, so we conclude that disregarding the hydrogen bond dynamics will only give rise to a slight peak broadening in the most important range. We will further concentrate on these details in future analysis of molecular vibrations in multi-tube systems.

We employed a central difference scheme to convert each of the extracted time traces of α to a time-dependent velocity of a (fantom) particle. Consequently, we calculated the cosine transform of the normalized velocity autocorrelation function for each particle. A Gaussian filter was applied to the whole time domain to avoid spurious signals in the frequency domain due to the truncation of the time signal at longer times. The resulting spectra for all 14 dimers are plotted in Figure A.17. It shows that all spectra share a number of bands, including one that is close to the experimentally relevant 145 cm^{-1}. We note that applying FFT directly to the time traces gives rise to a very similar band structure, but a much more noisy signal, hence we use the selected procedure via fantom particles.

APPENDIX B

Supporting Information for Chapter 3

Theoretical prediction of axial repeat distance d

We have extended the geometrical analysis introduced in Chapter 2 to account for a larger range of the chiral angle $\delta \in [0°, 180°]$ and an additional helical family. Using this analysis, the axial repeat distance d determined from the layer line position in the Fourier spectrum that was calculated from cryo-EM images can be related to the four main helical families, $H(1,0)$, $H(0,1)$, $H(1,1)$, $H(-1,1)$, as:

$$d_{\mathrm{H}(1,0)} = |\frac{b \sin\gamma}{\cos\delta}|$$

$$d_{\mathrm{H}(0,1)} = |\frac{a \sin\gamma}{\cos(\gamma-\delta)}|$$

$$d_{\mathrm{H}(1,1)} = |\frac{ab \sin\gamma}{a\cos(\delta) + b\cos(\gamma-\delta)}|$$

$$d_{\mathrm{H}(-1,1)} = |\frac{ab \sin\gamma}{a\cos(\delta) - b\cos(\gamma-\delta)}|$$

where the lattice parameters (a, b, γ) relate to unique properties of the dimeric unit cell. In particular, these four helical families can be seen as least sensitive to the disorder that will be present in experimental chlorosomes. When the denominator equals zero, the corresponding helical family constitutes lines parallel to the tube long axis.

The axial repeat distance d cannot be uniquely matched to a value in the

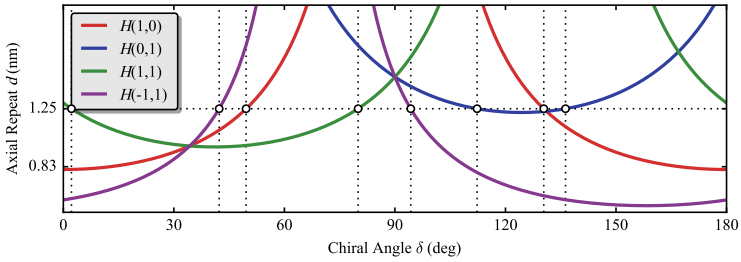

Figure B.1: The axial repeat d as a function of the chiral angle $\delta \in [0°, 180°]$ corresponding to the $H(1,0)$, $H(0,1)$, $H(1,1)$ and $H(-1,1)$ helical families. Since we are targeting the experimentally determined axial repeat distance d = 1.25 nm for WT chlorosomes, lattice parameters are set to $(1.48\text{ nm}, 0.98\text{ nm}, 124.3°)$ as determined from MD simulations of BChl *c* tubular assemblies (Chapter 2) to evaluate the geometrical relations. Matching chiral angles are highlighted by white circles.

δ-range, due to the uncertainty which of the main helical families relates to the experimental layer line. Yet, combining these relations and the lattice parameters (a, b, γ) extracted from AAMD simulations (Chapter 2), we can single out a small set of matching chiral δ for each experimentally determined axial repeat d. For wild-type (WT) chlorosomes, that are rich in BChl *c*, and mutant *bchQRU* chlorosomes rich in BChl *d*, the axial repeats d have been determined as 1.25 nm and 0.83 nm, respectively.[37] In particular, the lattice parameters were determined as $(1.48\text{ nm}, 0.98\text{ nm}, 124.3°)$ for pure BChl *c* aggregates and $(1.46\text{ nm}, 0.93\text{ nm}, 122.5°)$ for BChl *d* aggregates. Following this procedure, eight candidate chiral angles are found for WT chlorosomes, see Figure B.1: δ = 2.2 °, 42.3°,49.6°, 80.0°, 94.3°, 112.3°, 130.4° and 136.3°. For the *bchQRU* chlorosomes, only four candidate chiral angles match, see Figure B.2: δ = 19.8°, 27.6°, 108.9°, and 160.2°. For completeness, these values are summarized in Table 3.1.

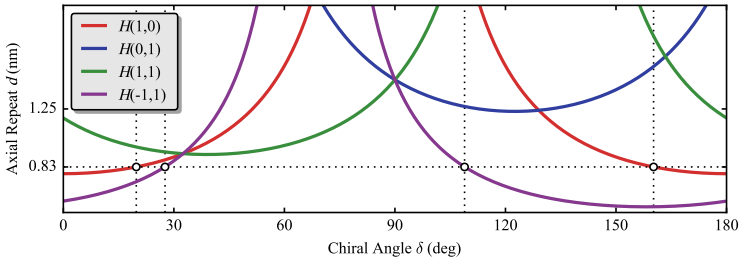

Figure B.2: The axial repeat d as a function of the chiral angle $\delta \in [0°, 180°]$ corresponding to the $H(1,0)$, $H(0,1)$, $H(1,1)$ and $H(-1,1)$ helical families. Since we are targeting the experimentally-determined axial repeat distance $d = 0.83$ nm for *bchQRU* chlorosomes, lattice parameters are set to $(1.46\text{ nm}, 0.93\text{ nm}, 122.5°)$ as determined from MD simulation of BChl *d* tubular assembly (Chapter 2). Matching chiral angles are highlighted by white circles.

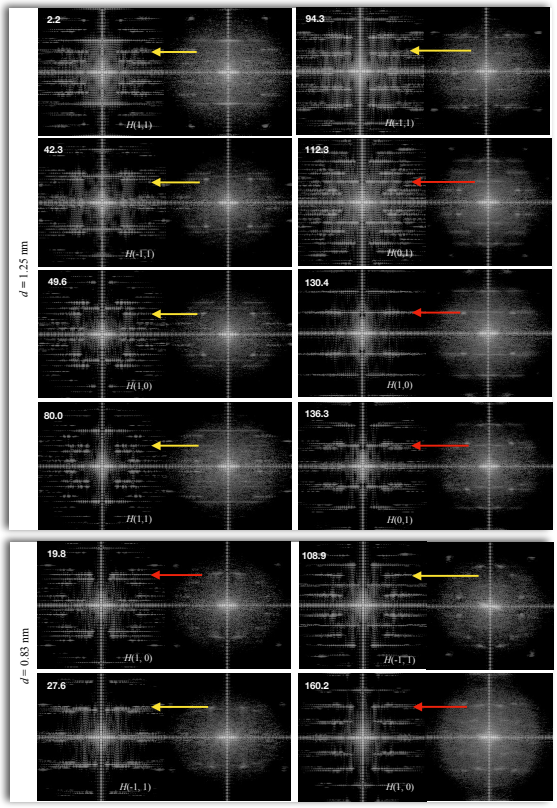

Figure B.3: EM mimics corresponding to tube structures for all δ that are listed in Table 3.1, with layer line positions at $1/d = 1/1.25$ nm^{-1} for WT or $1/d = 1/0.83$ nm^{-1} for *bchQRU* chlorosomes. For each δ, we show 2D power spectra for both the ordered structure at $T = 0$ K (left) and the structure after 1 ns MD simulation at ambient temperature, $T = 300$ K (right). The helical family corresponding to the target layer line is given at the right bottom in the 0 K spectrum. Arrows point to the target layer lines from our geometrical analysis: red indicates a meridian signal that is consistent with the diffraction pattern observed in experiments, while yellow indicates a signal further away from the meridian or a missing signal due to structural disorder. The diffraction patterns of the 2D power spectra for the structures after MD simulation at $T = 300$ K are used for a realistic comparison to experimental diffraction data. 2D power spectra are calculated for single tubes of 40 nm length, using a procedure that is described in Chapter 2. For clarity, the contrast of each diffraction pattern is increased by 25%. We note the same diffraction pattern of 112.3° is found for 105°, including the meridian signal characteristics.

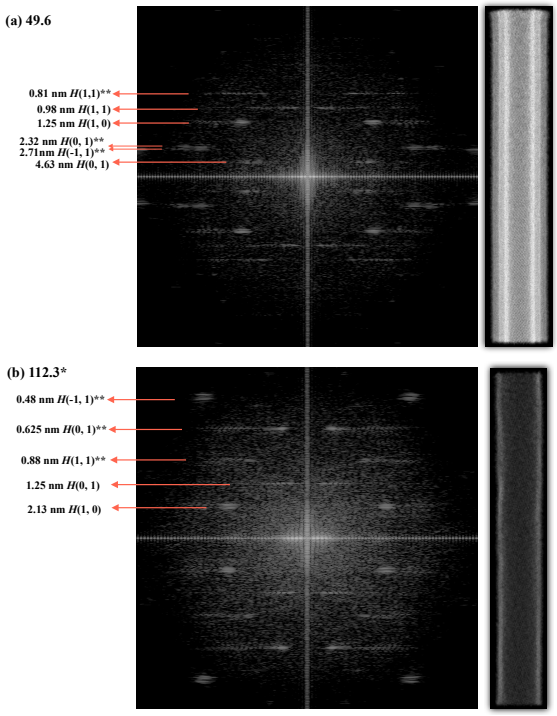

Figure B.4: Left: 2D power spectra for the $\delta = 49.6°$ (a, concentric) and $\delta = 112.3^*$ (b, single) tube structures. Layer lines are labeled by the helical family and the corresponding repeat distance. Spectra are calculated for 120 nm long tubes after 1 ns MD simulation at ambient temperature, *i.e.* $T = 300$ K, shown at the right in terms of the 2D projection of the electron density. Layer lines with strong signals denoted by superscript ** originate from a lattice with half the **a** dimension of the unit cell, which corresponds to the distance between *syn* and *anti*. It shows that *syn* and *anti* cannot always be distinguished in electron diffraction. For clarity, the contrast of each diffraction pattern is increased by 25%.

Table B.1: Small- and large-scale structural properties of pre-assembled structures at different stages of preparation and simulation: after energy minimization (0 K), after 1 ns MD simulation at 50 K and subsequent 1 ns at 300 K. MD simulations were carried out in an NVT ensemble for structures that were pre-assembled for matching δ, following the procedure described in the Method section 3.2. In all cases, only Mg atoms in N molecules are considered for the determination of structural properties, which include local packing parameters (a, b, γ), calculated as an average over the whole structure, and large-scale features like the adopted chiral angle δ and tube radius R which were determined from a best least-square fit. Standard deviations and residuals of this fitting procedure are included.

	$\delta_{\text{ideal}}(^\circ)$	N	label(K)	a(nm)	b(nm)	$\gamma(^\circ)$	$\delta_{\text{fit}}(^\circ)$	R_{fit}(nm)	RMSD_{fit}(nm)
wild type $\delta_{1,25}$	2.2	9272	0	1.48 ± 0.0	0.98 ± 0.0	124.0 ± 0.07	2.0 ± 0.0	7.39	0.02
			50	1.49 ± 0.02	0.98 ± 0.03	125.3 ± 1.8	2.3 ± 0.0	7.41	0.15
			300	1.49 ± 0.03	0.99 ± 0.04	123.2 ± 3.19	2.7 ± 0.01	7.36	0.22
	42.3	9397	0	1.48 ± 0.0	0.98 ± 0.0	124.3 ± 0.06	42.2 ± 0.0	7.48	0.01
			50	1.49 ± 0.02	0.98 ± 0.03	125.0 ± 1.96	41.8 ± 0.04	7.39	0.11
			300	1.49 ± 0.03	0.99 ± 0.04	124.0 ± 2.86	42.2 ± 0.08	7.5	0.21
	49.6	9144	0	1.48 ± 0.0	0.98 ± 0.0	124.3 ± 0.06	49.7 ± 0.0	7.28	0.01
			50	1.5 ± 0.02	0.97 ± 0.03	125.0 ± 1.99	48.9 ± 0.05	7.18	0.11
			300	1.5 ± 0.03	0.99 ± 0.04	123.9 ± 2.9	49.4 ± 0.07	7.3	0.17
	80.0	8068	0	1.48 ± 0.0	0.98 ± 0.0	124.3 ± 0.04	80.0 ± 0.0	6.41	0.0
			50	1.49 ± 0.02	0.98 ± 0.03	125.0 ± 2.0	80.3 ± 0.08	6.3	0.11
			300	1.49 ± 0.03	1.0 ± 0.04	123.6 ± 3.0	80.2 ± 0.13	6.48	0.2
	94.3	9253	0	1.48 ± 0.0	0.98 ± 0.0	124.3 ± 0.03	94.2 ± 0.0	7.37	0.0
			50	1.49 ± 0.02	0.98 ± 0.03	125.1 ± 2.0	95.3 ± 0.06	7.28	0.15
			300	1.49 ± 0.03	1.0 ± 0.05	123.3 ± 3.29	94.6 ± 0.16	7.45	0.29
	112.3	9468	0	1.48 ± 0.0	0.98 ± 0.0	124.2 ± 0.04	112.4 ± 0.0	7.53	0.0
			50	1.48 ± 0.02	0.99 ± 0.03	125.1 ± 2.03	113.9 ± 0.07	7.53	0.17
			300	1.48 ± 0.03	1.0 ± 0.05	123.0 ± 3.37	112.2 ± 0.17	7.6	0.29
	130.4	9161	0	1.48 ± 0.0	0.98 ± 0.0	123.9 ± 0.05	130.5 ± 0.0	7.29	0.01
			50	1.48 ± 0.02	0.98 ± 0.03	125.1 ± 1.88	131.8 ± 0.04	7.31	0.13
			300	1.48 ± 0.03	1.0 ± 0.05	122.6 ± 3.51	130.1 ± 0.11	7.31	0.26
	136.3	9392	0	1.48 ± 0.0	0.98 ± 0.0	123.9 ± 0.05	136.4 ± 0.0	7.48	0.01
			50	1.49 ± 0.02	0.98 ± 0.03	125.3 ± 1.91	137.7 ± 0.06	7.52	0.13
			300	1.48 ± 0.03	1.0 ± 0.05	122.6 ± 3.55	136.0 ± 0.17	7.47	0.3
bchQRU $\delta_{0,83}$	19.8	8766	0	1.46 ± 0.0	0.93 ± 0.0	122.4 ± 0.05	19.7 ± 0.0	6.63	0.02
			50	1.48 ± 0.03	0.93 ± 0.03	122.3 ± 2.44	19.3 ± 0.03	6.69	0.22
			300	1.47 ± 0.05	0.94 ± 0.04	120.8 ± 3.71	19.7 ± 0.03	6.65	0.29
	27.6	8844	0	1.46 ± 0.0	0.93 ± 0.0	122.5 ± 0.06	27.6 ± 0.0	6.71	0.02
			50	1.48 ± 0.03	0.92 ± 0.03	122.5 ± 2.47	26.8 ± 0.08	6.76	0.24
			300	1.47 ± 0.05	0.94 ± 0.04	120.7 ± 3.88	27.6 ± 0.07	6.71	0.32
	108.9	8858	0	1.46 ± 0.0	0.93 ± 0.0	122.4 ± 0.04	109.0 ± 0.0	6.71	0.0
			50	1.51 ± 0.02	0.91 ± 0.02	122.3 ± 2.19	108.3 ± 0.11	6.5	0.21
			300	1.48 ± 0.06	0.94 ± 0.05	119.5 ± 4.12	106.6 ± 0.32	6.65	0.6
	160.2	9289	0	1.46 ± 0.0	0.93 ± 0.0	122.0 ± 0.11	160.4 ± 0.0	7.05	0.02
			50	1.47 ± 0.03	0.93 ± 0.02	123.2 ± 2.62	161.0 ± 0.02	7.1	0.19
			300	1.46 ± 0.04	0.94 ± 0.04	120.3 ± 3.99	160.1 ± 0.04	6.91	0.51

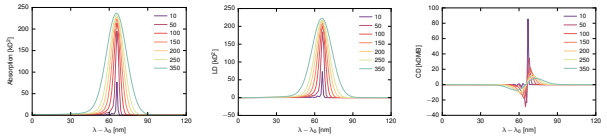

(a) 120 nm

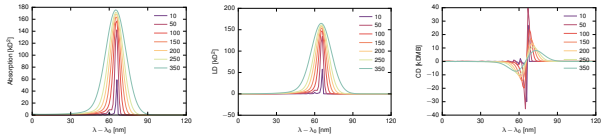

(b) 90 nm

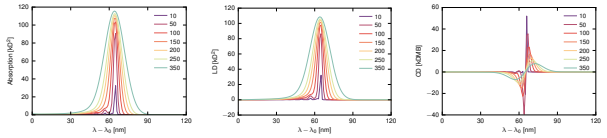

(c) 60 nm

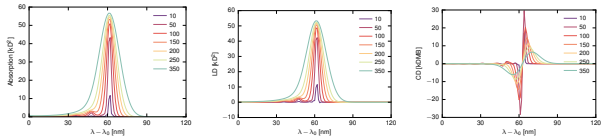

(d) 30 nm

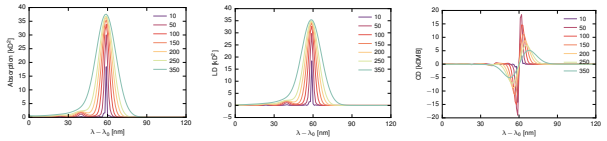

(e) 20 nm

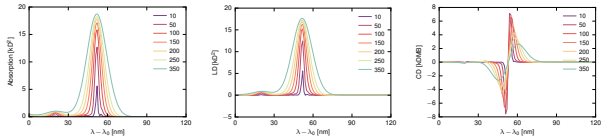

(f) 10 nm

Figure B.5: Spectral plots for the tube at 300 K after 1ns MD simulation for $\delta = 49.6°$, *i.e.* one of the two matching chiral angles for BChl *c*-rich aggregates like the WT chlorosome. Different tube lengths have been considered, from very short 10 nm tubes to the longest 120 nm. We have convolved stick spectra with Gaussians that feature a range of FWHM values, from 10 to 350 cm^{-1}, to evaluate the broadening effect. In particular, the effect of homogeneous and heterogeneous broadening has been shown to vary in experimental spectra.

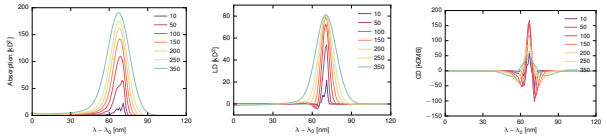

(a) 120 nm

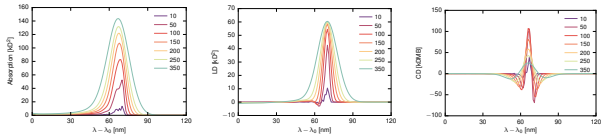

(b) 90 nm

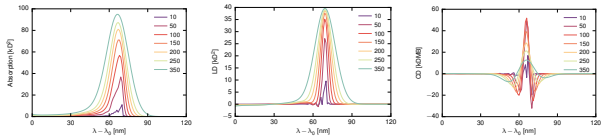

(c) 60 nm

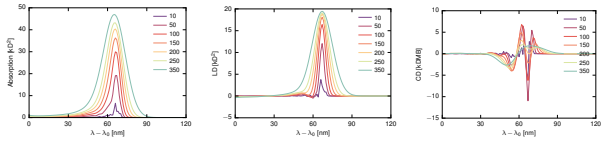

(d) 30 nm

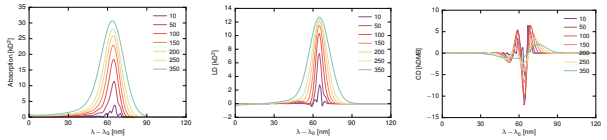

(e) 20 nm

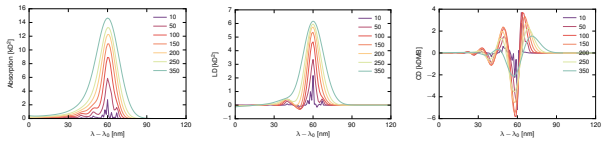

(f) 10 nm

Figure B.6: Spectral plots for the tube at 300 K after 1 ns MD simulation for $\delta = 19.8°$, *i.e.* one of the two matching chiral angles for BChl *d*-rich assembles like the mutant *bchQRU* chlorosome. Different tube lengths have been considered, from very short 10 nm tubes to the longest 120 nm. We have convolved stick spectra with Gaussians that feature a range of FWHM values, from 10 to 350 cm^{-1}, to evaluate the broadening effect. In particular, the effect of homogeneous and heterogeneous broadening has been shown to vary in experimental spectra.

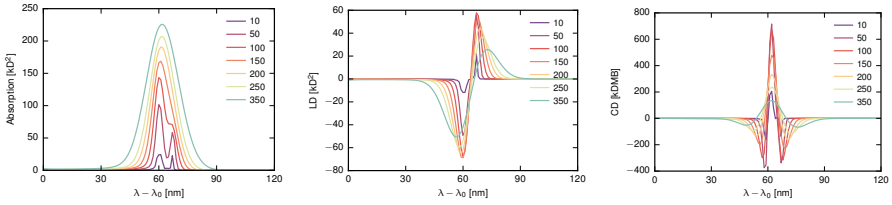

(a) 2.2

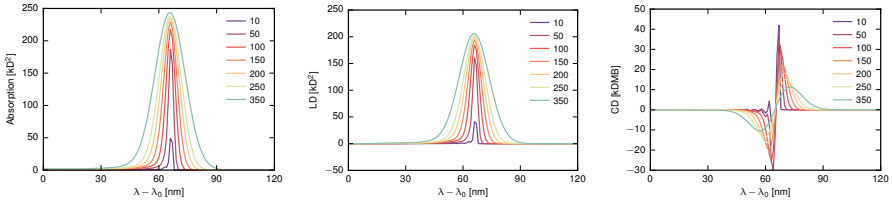

(b) 42.3

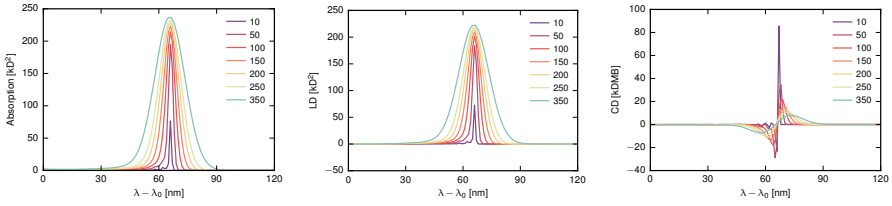

(c) 49.6

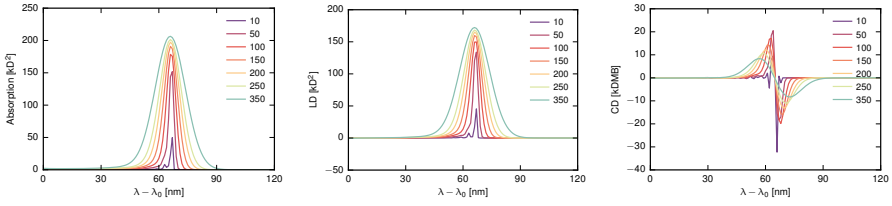

(d) 80.0

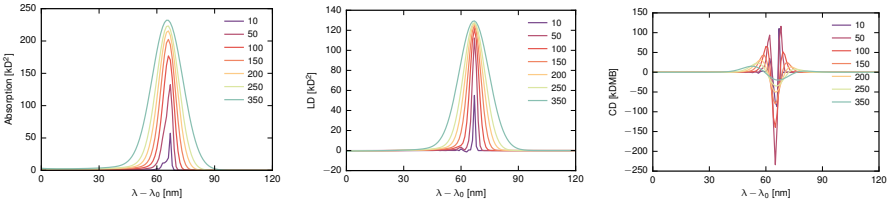

(e) 94.3

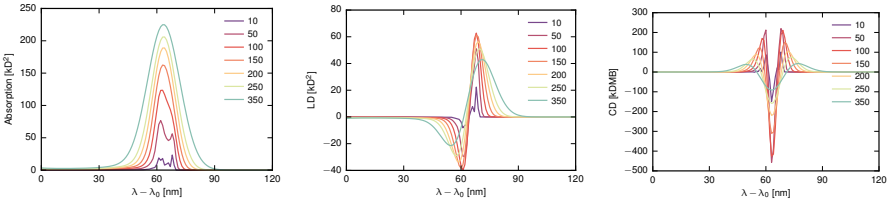

(f) 112.3

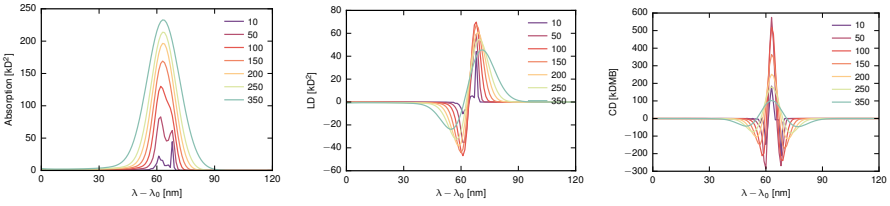

(g) 112.3*

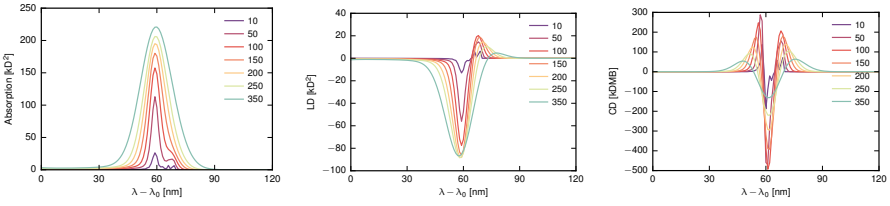

(h) 130.4

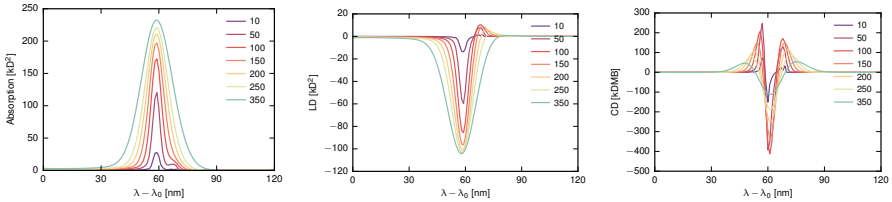

(i) 136.3

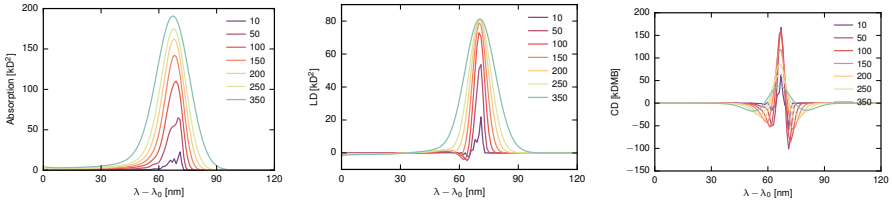

(j) 19.8

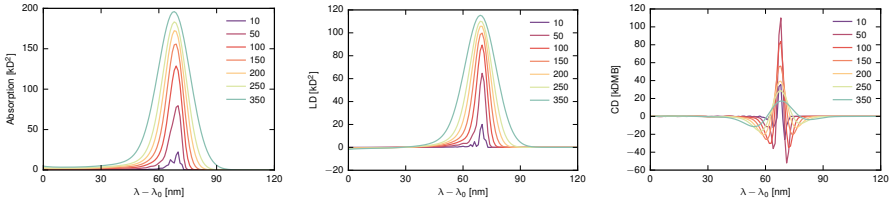

(k) 27.6

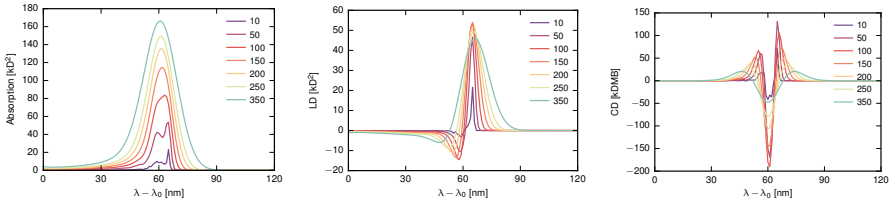

(l) 108.9

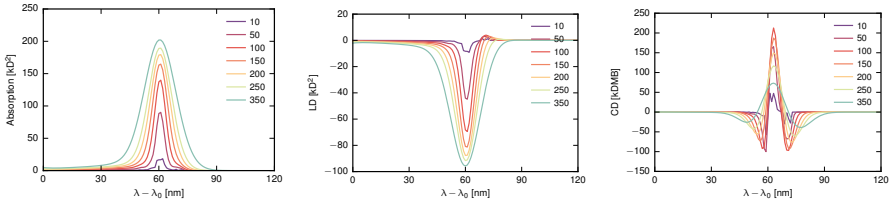

(m) 160.2

Figure B.7: Spectral plots for all tube structures with matching δ at 300 K. We have convolved stick spectra with Gaussians that feature a range of FWHM values, from 10 to 350 cm^{-1}, to evaluate the broadening effect. In particular, the effect of homogeneous and heterogeneous broadening has been shown to vary in experimental spectra.

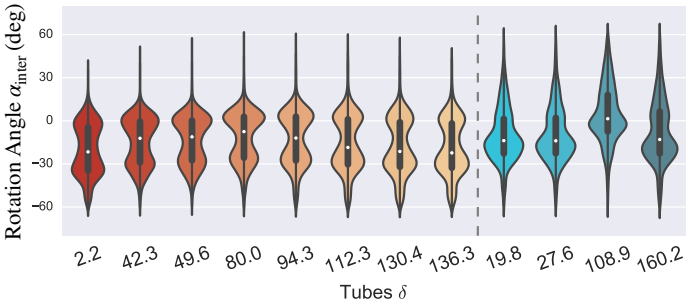

Figure B.8: Sampling distribution for the relative head-head rotation angle between *anti* and *syn* molecules BChl, α_{inter}, for the tube obtained after 1 ns MD simulation at 300 K. The distribution is calculated for different chiral angles δ on the horizontal axis, and the dashed line separates the matching chiral angles for BChl *c* and *d*. We refer to the main text, figure 3.4, for the distribution of α_{intra}.

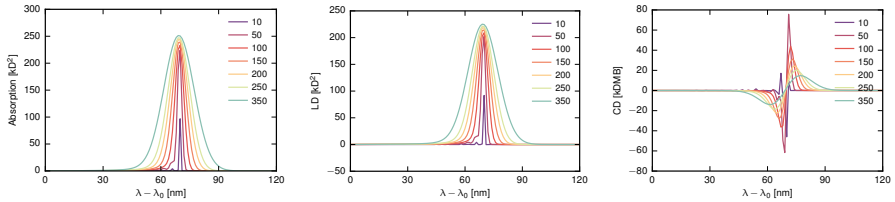

(a) 0 K

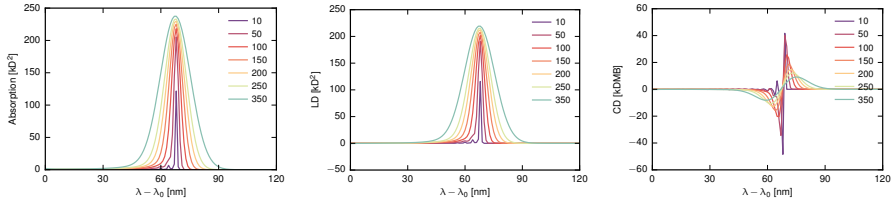

(b) 50 K

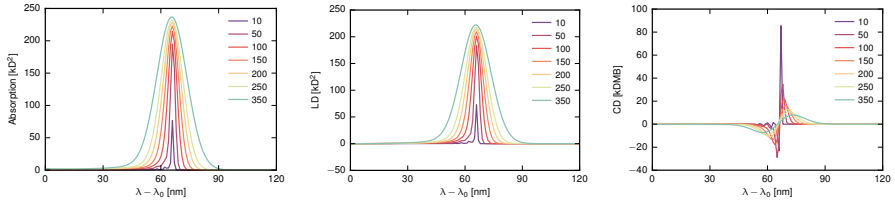

(c) 300 K

Figure B.9: Spectral plots for the tube that was pre-assembled for $\delta = 49.6°$, at different stages of preparation/simulation: 0 K, 50 K and 300 K. We have convolved stick spectra with Gaussians that feature a range of FWHM values, from 10 to 350 cm^{-1}, to evaluate the broadening effect. In particular, the effect of homogeneous and heterogeneous broadening has been shown to vary in experimental spectra.

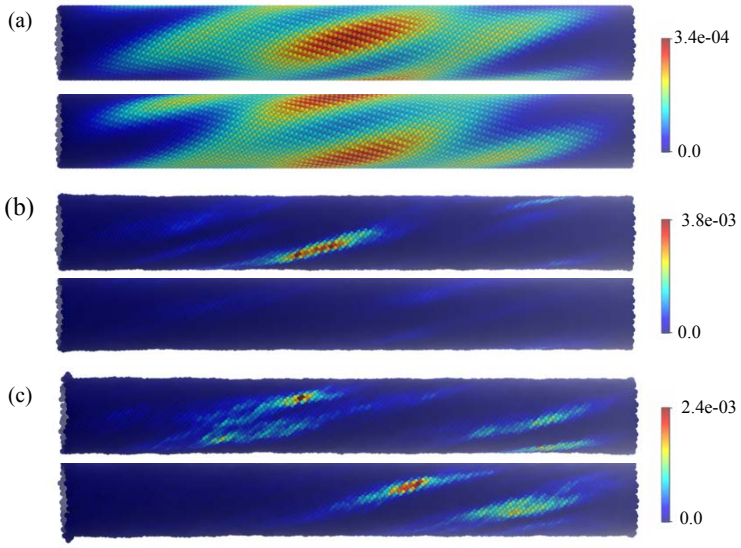

Figure B.10: Spatial distribution of the exciton states with the highest oscillator strength ψ_{max} in a 120 nm long tube for a matching $\delta = 49.6°$. From top to bottom: ψ_{max} for different disorder within the tube: ordered state (a), and disordered states after 1 ns MD simulation at 50 K (b) and 300 K (c). In each case, the front and back view of the tube are both shown. Tube structures also have been unrolled to planar ones for the purpose of visualization, see Figure 3.6.

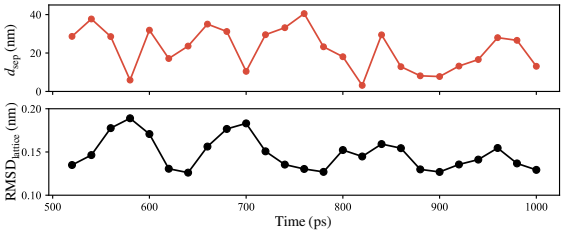

Figure B.11: Analysis of the structural and exciton state variation along a long 500 ps MD trajectory for a tube with $\delta = 49.6°$. Top: Time evolution of d_{sep}, the distance between molecules associated with the largest exciton density in ψ_{max} in consecutive frames. Bottom: RMSD for the lattice between consecutive frames, calculated from the Mg positions.

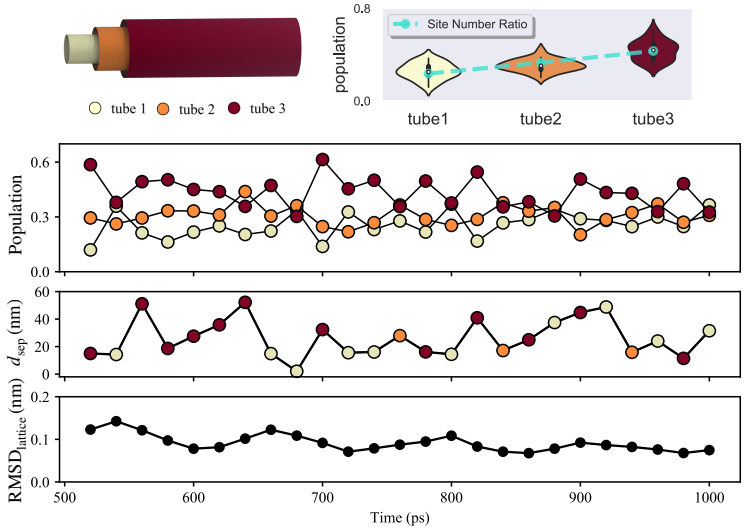

Figure B.12: Analysis of structural and excitons state variation of ψ_{max} in concentric 3-tube structures along a long 500 ps trajectory. From top to bottom: (left) Schematic illustration of concentric tube geometry, with radii satisfying tube 3 > tube 2 > tube 1. Colors are used to distinguish between different tubes. (right) Distribution of exciton density population of ψ_{max} over all frames in the trajectory. The average (white point) agrees well with the trend of the normalized number of molecules (site number ratio, dashed line) in each tube. Below: The exciton density population in different tubes, denoted by tube color, along a 1 ps trajectory. Below: d_{sep}, the distance between molecules associated with the largest exciton density in ψ_{max} in consecutive frames. Color specifies in which tube the molecule with the highest exciton density is situated. Bottom: RMSD for the lattice between consecutive frames, calculated from the Mg positions.

APPENDIX C

Supporting Information for Chapter 4

Computational Details

AAMD simulation. The tube studied in this work is composed of *syn-anti* dimers of BChl *c* molecules. For MD force field details for the BChl *c* molecule, we refer to Chapter 2. We give a brief summary here. The OPLS-AA force field[92] was used for all simulations. Charge parameters were refined by the RESP method.[94] In the pigment head part, four Mg–N bonds were added to keep the Mg atom stable within the ring. Electrostatic interactions were calculated by a particle-mesh Ewald method.[98] MD simulations with periodic boundary conditions along all dimensions were conducted using the Gromacs software (version 2016.1).[97] We performed NVT simulations, maintaining the temperature by the velocity-rescaling thermostat.[99]

Helical Tube MD trajectory. We briefly summarize the protocol for obtaining a stable tube structure, and refer to Chapters 3 and 5 for more details. A tube structure for a specific chiral angle was first packed using a in-house code. To alleviate any possible unfavored geometrical overlap, and to ensure stable MD simulation, we first performed steepest descent optimization, then performed constrained MD simulation keeping the head part fixed and sequentially only the Mg atoms, followed by MD simulation without constraints at 50 K (1 ns). After this equilibration, we performed MD simulation at 300 K and collected snapshots of the nuclear coordinates every 20 fs along a 1 ps MD trajectory. There snapshots were used to calculate the Frenkel Hamiltonians.

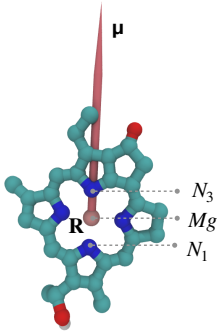

Figure C.1: Molecular detail of the determination of the transition dipole $\boldsymbol{\mu}$ from a BChl *c* molecule. The director (shown by a red arrow) is given by the vector connecting the two indicated Nitrogen atoms, with origin given by the coordinates of the Mg atom (shown by a pink sphere). The magnitude $|\boldsymbol{\mu}|$ of this vector is 5.48 D, as estimated from experiments. The tail part of the molecule and most hydrogen atoms are omitted for visual clarity.

Frenkel Hamiltonian Parameterization. We briefly summarize how the Frenkel Hamiltonian is calculated. For more details and discussions, we refer to Chapter 3. As shown in Eq.4.1, the Hamiltonian is a 2D matrix composed of diagonal (site energy) and off-diagonal (electronic coupling) terms. For the site energy, we considered a constant monomer excitation energy of a BChl *c* pigment molecule: $\nu = 15390$ cm^{-1} for the Q_y-transition of isolated BChl *c* in methanol.[80] The J_{ij}, representing the electronic coupling between molecules i and j, is calculated via the standard point-dipole approximation (PDA),[122]

$$J_{ij}(\boldsymbol{\mu}_i(t), \boldsymbol{\mu}_j(t), \mathbf{R}_{ij}(t)) = \frac{\boldsymbol{\mu}_i \cdot \boldsymbol{\mu}_j}{\left|\mathbf{R}_{ij}\right|^3} - 3\frac{(\boldsymbol{\mu}_i \cdot \mathbf{R}_{ij})(\boldsymbol{\mu}_j \cdot \mathbf{R}_{ij})}{\left|\mathbf{R}_{ij}\right|^5} . \tag{C.1}$$

For a give BChl *c* molecule, the transition dipole moment vector $\boldsymbol{\mu}$ is oriented along the vector connecting two Nitrogen atoms, see FigureC.1. The magnitude $|\boldsymbol{\mu}|$ of this vector is 5.48 D, as estimated from experimental data.[124] The transition dipole moment vector $\boldsymbol{\mu}$ is placed at the position of the Mg atom $\mathbf{R}$ in the molecule, see FigureC.1. $\mathbf{R}_{ij}$ is the distance vector between two transition

dipoles at positions $\mathbf{R}_i$ and $\mathbf{R}_j$. Within this PDA treatment, only three atoms in a molecule are relevant for the electronic coupling terms.

Definition of Different Domain Properties. As shown in Figure C.7, we calculated several properties of the domains and checked their correlation with P_{domain}, for instance, the positive (J^{+}_{domain}) and negative (J^{-}_{domain}) part of J_{domain}, rotation angle (α) and distance (d) between neighboring transition dipoles.

- J_{domain} is the overall electronic coupling strength in the domain, see Eq. C.1;
- J^{+}_{domain} is defined as

$$J^{+}_{\text{domain}} = \sum_{i,j \in \text{domain}, i \neq j} \frac{\boldsymbol{\mu}_i \cdot \boldsymbol{\mu}_j}{\left|\mathbf{R}_{ij}\right|^3}; \tag{C.2}$$

- J^{-}_{domain} is defined as

$$J^{-}_{\text{domain}} = - \sum_{i,j \in \text{domain}, i \neq j} 3\frac{(\boldsymbol{\mu}_i \cdot \mathbf{R}_{ij})(\boldsymbol{\mu}_j \cdot \mathbf{R}_{ij})}{\left|\mathbf{R}_{ij}\right|^5} \tag{C.3}$$

- α is the average neighboring dipole-dipole rotation angle along the **a** packing direction; d is the average neighboring Mg-Mg distance (equivalent to the dipole-dipole distance) along the **a** packing direction. Such properties were also discussed before in Chapter 3. Neighboring transition dipoles are selected via a distance constraint with a threshold of 0.8 nm. Following such a rule, molecules along the *syn-anti* packing direction, *i.e.* helices from the (1, 0) helical family (see Chapter 3), are considered.

Exciton dynamics. The details of our exciton dynamics simulations are summarized in Scheme C.1.

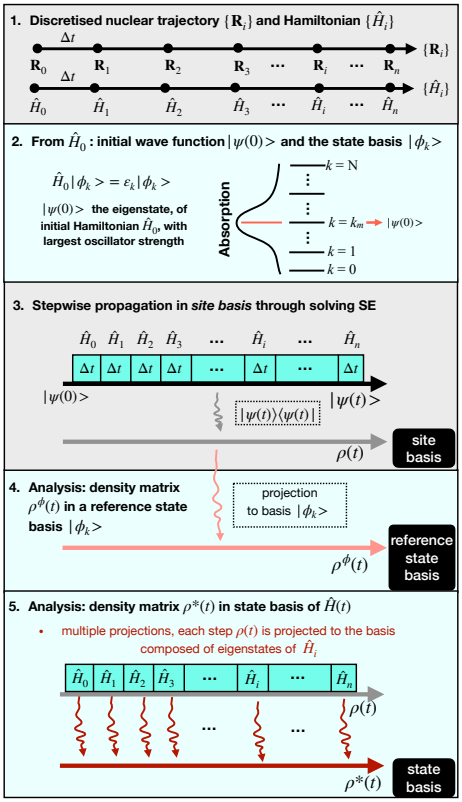

Scheme C.1: Schematic representation of the exciton dynamics simulation setup. (1) The time dependent Hamiltonian $\hat{H}(t)$ is updated every $\Delta t = 20 fs$ according to the molecular conformations $\mathbf{R}_t$ from MD trajectory that define transition dipoles and origins $\{\boldsymbol{\mu}, \mathbf{R}\}$(shown in Figure C.1). (2) The initial wave function $|\psi(0)\rangle$ is an eigenstate of the Hamiltonian $\hat{H}_0 = \hat{H}(t = 0)$. We select the eigenstates $|\phi_k\rangle$ as the reference state basis in the following analysis. (3) SE represents the time dependent Schrödinger equation. Within each $\Delta t = 20$ fs time interval, the Hamiltonian is treated as a constant, and the wave function is propagated unitarily with a time step of 1 fs, through solving a SE equation using the "zvode" ODE solver implemented in QUTIP software. (4) Along the exciton dynamics trajectory, we collected the wave function $|\psi(t)\rangle$ and density matrix $\rho(t)$ in the site basis. For analysis, through applying projection from the site basis to a reference state basis of $\hat{H}_0$, we obtained the density matrix $\rho^{\phi}(t)$ in the state basis $|\phi_k\rangle$. (5) For additional analysis, we also projected the density matrix $\rho^{\phi}(t)$ to the state basis of $\hat{H}(t)$, through multiple projections. To evaluate our choice of $\Delta t = 20$ fs, we considered a static case, where the Hamiltonian $\hat{H}_1$ is constant, computed from the molecule conformation $\mathbf{R}_1$ at $t = 20$ fs taken from the MD trajectory. In such a case, the exciton dynamics is governed by the SE, $i\hbar \frac{\partial}{\partial t}|\psi(t)\rangle = \hat{H}_1|\psi(t)\rangle$.

Extra plots

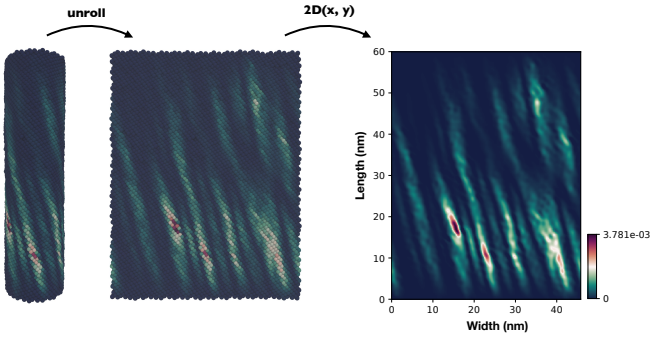

Figure C.2: Spatial distribution of a wave function projected on molecules in tube (left), after unrolling to a planar representation (middle) and subsequent smoothing to a fine 2D grid (right). The resolution of the grid in the smoothed 2D surface is set to 0.5 Å, interpolated using a multi-quadric radial basis function.

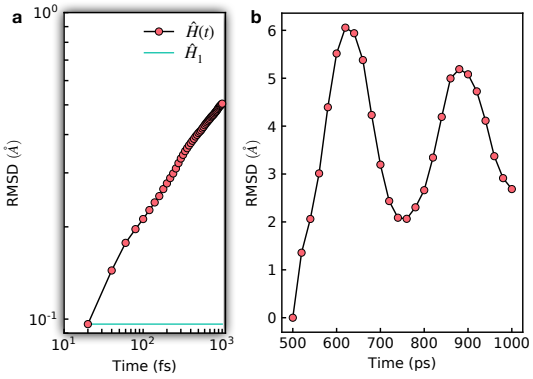

Figure C.3: (a) RMSD of the nuclear coordinates of the two Nitrogen and the Mg atoms that define the transition dipoles in the Hamiltonian for either the $\hat{H}(t)$ and constant $\hat{H}_1$ cases, see Figure C.1.The constant RMSD ≈ 0.1Å for the nuclear coordinates used in $\hat{H}_1$ are denoted by a horizontal line. Coordinates at $t = 0$ is used as the reference. (b) Plot of the RMSD for a extended 500 ps trajectory, clearly showing that on a longer time scale there is no free diffusion but oscillatory behavior with a periodicity of about 250 ps.

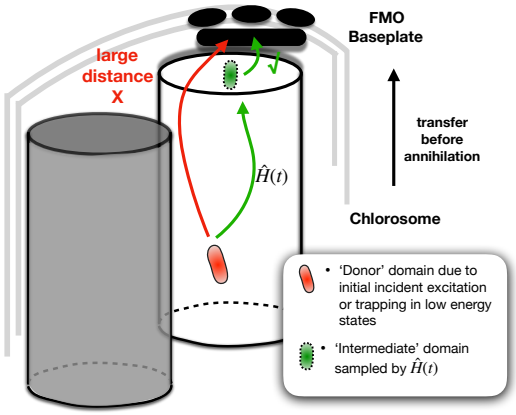

Scheme C.2: Schematic representation of a possible spatial barrier in the energy transfer process from the chlorosome to a sink, *i.e.* baseplate and FMO, in photosynthetic bacteria. When the 'acceptor' in the baseplate/FMO is far away from the 'donor' domain, in the $\hat{H}(t)$ case the dynamic disorder may introduce an 'intermediate' domain that is close enough to the 'acceptor' to enable hopping by a Förster-like mechanism. If consider the Förster mechanism, proximity is key, since its efficiency is inversely proportional to the sixth power of this distance. We note that, if the exciton Hamiltonian also includes the baseplate/FMO, the 'acceptor' domain may be sampled directly.

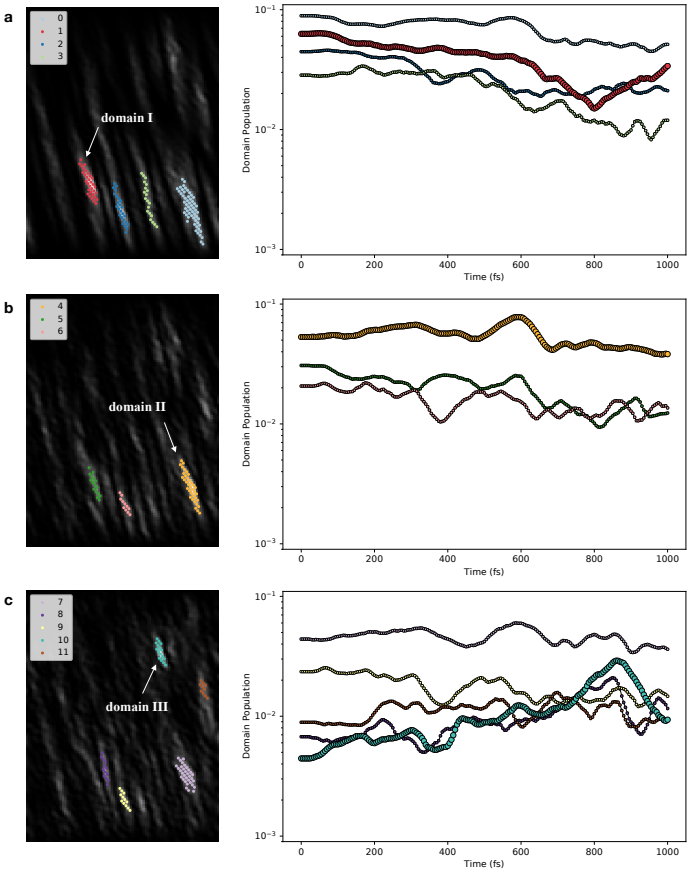

Figure C.4: (left) Tube domains identified from snapshots at 0 (a), 600 (b) and 865 (c) fs, and (right) corresponding domain populations $P_{\text{domain}}(t)$ for the Hamiltonian with dynamic disorder, *i.e.* the $\hat{H}(t)$ case. Domains were obtained via the DBSCAN clustering algorithm.[233] Each domain is assigned to a specific number and a color.

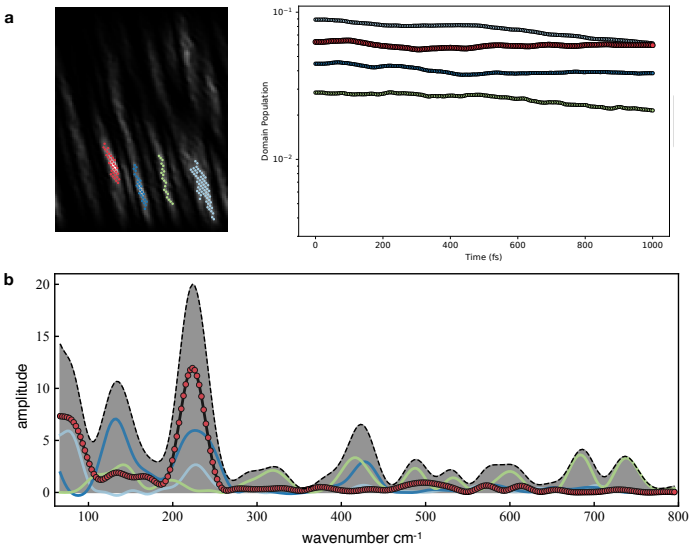

Figure C.5: Analysis for the constant $\hat{H}_1$ case: (a) domains identified at $t = 0$ fs (left) and evolution of the domain population along the 1 ps exciton dynamics trajectory (right). (b) Fourier spectra (amplitude versus wavenumber) calculated from the time traces of the domain populations. Domain I is highlighted by red color. The gray shadow plot shows the average amplitude of different domain cases. For visual clarify, the maximum value in the average amplitude plot is scaled to 20. Frequencies corresponding to time scales longer than half of the exciton trajectory of 1 ps are not shown.

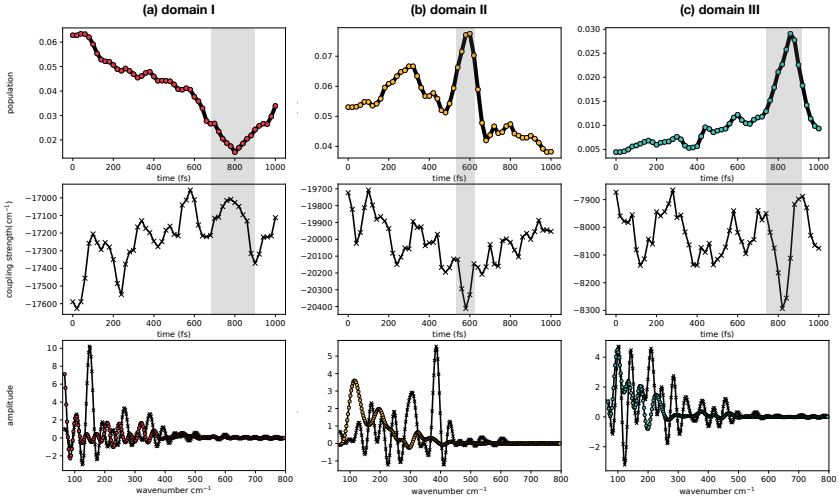

Figure C.6: Comparison of domain properties for the $\hat{H}(t)$ case: domain population P_{domain}(top) and electronic coupling strength J_{domain}(middle) along the exciton trajectory, and the FFT spectral analysis (bottom) of P_{domain} and J_{domain} for domain I (a), II (b) and III (c). The calculated cross-correlations between P_{domain} and J_{domain} (with zero lag) for domain I (a), II (b) and III are –0.61, –0.34, and –0.21 respectively. Frequencies corresponding to time scales longer than half of the exciton trajectory of 1 ps are not shown.

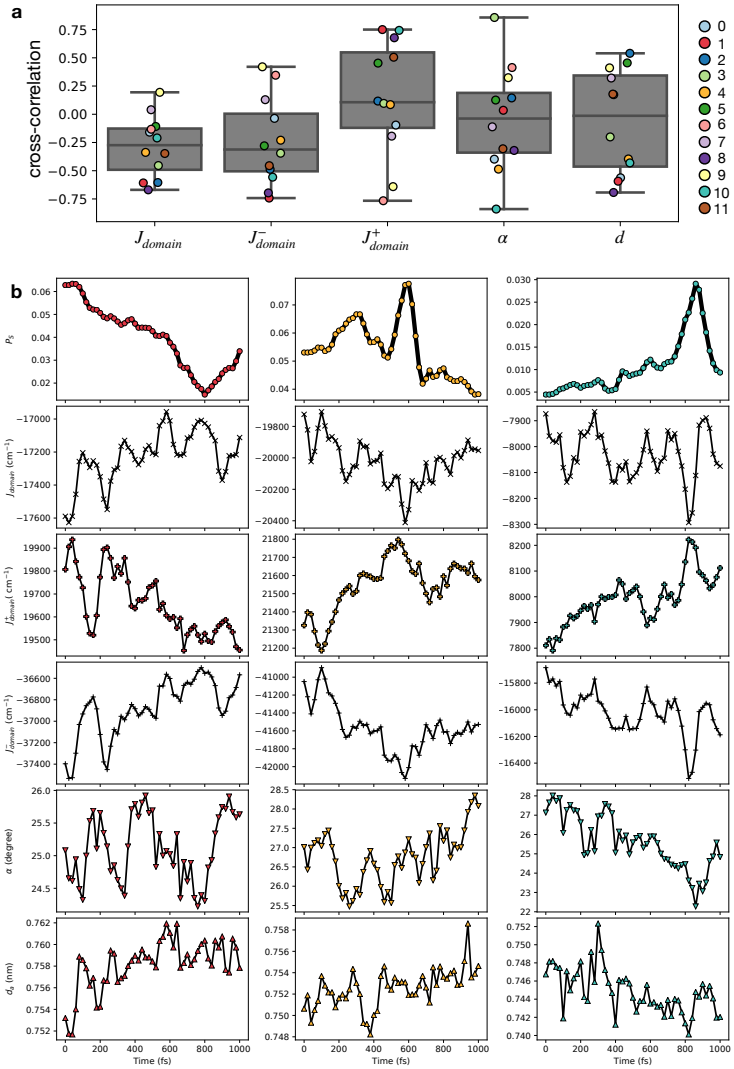

Figure C.7: Domain properties for the $\hat{H}(t)$ case: P_{domain}, J_{domain}, J^{+}_{domain}, J^{-}_{domain}, α and d. (a) Box plot of cross-correlation values between P_{domain} and all other properties for all domains. Domains are labeled by the same color code as in Figure C.4. The domain indices for domain I, II and III are 1, 4 and 10 respectively. (b)Time traces of the examined domain properties for domains I, II and III.

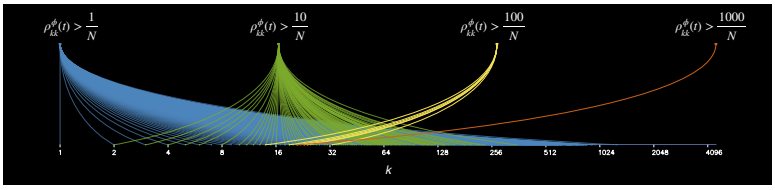

Figure C.8: Collection of states in the reference state basis that satisfy the following population threshold: $\rho^{\phi}_{kk}(t) > \frac{1}{N}, \frac{10}{N}, \frac{100}{N}$ or $\frac{1000}{N}$. States that satisfy this selection rule are connected.

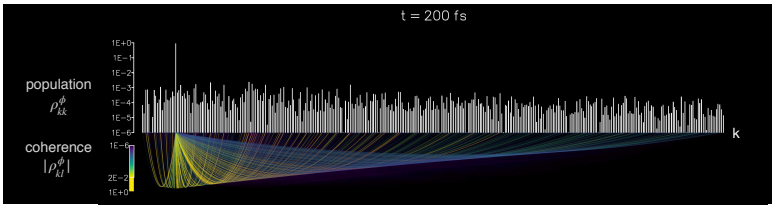

Figure C.9: Visualization of the k < 350 part of the density matrix ρ^{ϕ} in the reference state basis $|\phi_k\rangle$ at t = 200 fs. Top part: the magnitude of diagonal elements of the density matrix ρ^{ϕ}_{kk} are visualized as vertical lines. Bottom part: the relative magnitude of off-diagonal terms $|\rho^{\phi}_{kl}|$ are visualized via coloring of the arc curve connecting the k and l in the x-axis. On the x-axis, the state number k is arranged from low to high. For clear visualization in the color plot, the transparency (alpha parameter in RGBA color) of an arc curve is set to $20 * |\rho^{\phi}_{kl}|$, where 0 is completely transparent and 1 not transparent at all. The plots are made using PyCardio package (https://github.com/obarquero/PyCardio).

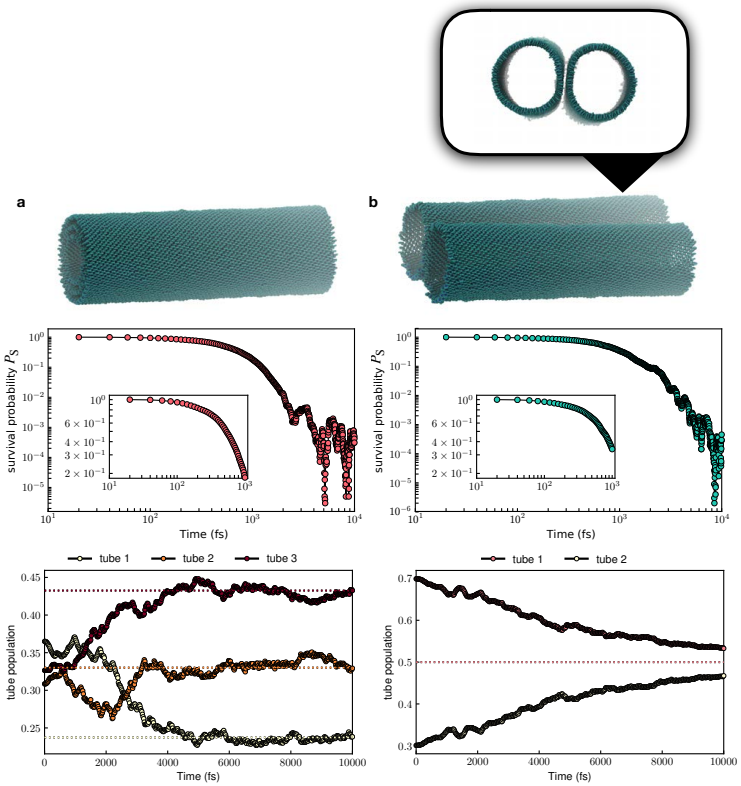

Figure C.10: Analysis of excitonic properties for tubular assemblies with different connectivities: concentric tubes (a) and side-by-side aligned tubes (b). Top: atomistic structures, middle: the initial state survival probability $P_S(t)$, and bottom: the tube population $P_{\text{tube}}(t)$ along the 10 ps exciton dynamics trajectories. As outlined in Scheme C.1, the initial wave function $|\psi(0)\rangle$ is selected as the absorption state of the whole assembly. The orthographic view of the tube assembly in inset of (b) shows that the tubes deform in the contact area.

Bibliography

(1) Scholes, G. D.; Fleming, G. R.; Olaya-Castro, A.; Van Grondelle, R. *Nat. Chem.* **2011**, *3*, 763–774.
(2) Croce, R.; Van Amerongen, H. *Nat. Chem. Biol.* **2014**, *10*, 492–501.
(3) Muller, P.; Li, X.; Niyogi, K. *Plant Physiol.* **2001**, *125*, 1558–1566.
(4) Barber, J. *Chem. Soc. Rev.* **2009**, *38*, 185–196.
(5) Magdaong, N. C. M.; Blankenship, R. E. *J. Biol. Chem.* **2018**, *293*, 5018–5025.
(6) Bryant, D. A.; Canniffe, D. P. *J. Phys. B: At. Mol. Opt. Phys.* **2018**, *51*, 033001.
(7) Zuber, H. *Trends Biochem.Sci.* **1986**, *11*, 414–419.
(8) Mirkovic, T.; Ostroumov, E.; Anna, J. M.; Van Grondelle, R.; Govindjee; Scholes, G. D. *Chem. Rev.* **2017**, *117*, 249–293.
(9) Yurkov, V.; Beatty, J. *Microbiol. Mol. Biol. Rev.* **1998**, *62*, 695.
(10) Imhoff, J. F., *Biology of Green Sulfur Bacteria. In: eLS*; John Wiley & Sons, Ltd: Chichester: 2014.
(11) Overmann, J.; Cypionka, H.; Pfennig, N. *Limnol. Oceanogr.* **1992**, *37*, 150–155.
(12) Beatty, J. T.; Overmann, J.; Lince, M. T.; Manske, A. K.; Lang, A. S.; Blankenship, R. E.; Van Dover, C. L.; Martinson, T. A.; Plumley, F. G. *Proc. Natl. Acad. Sci. U. S. A.* **2005**, *102*, 9306–9310.
(13) Olson, J. M. *Photochem. Photobiol.* **1998**, *67*, 61–75.
(14) Pšenčík, J.; Arellano, J. B.; Ikonen, T. P.; Borrego, C. M.; Laurinmäki, P. A.; Butcher, S. J.; Serimaa, R. E.; Tuma, R. *Biophys. J.* **2006**, *91*, 1433–1440.
(15) Oostergetel, G. T.; Van Amerongen, H.; Boekema, E. J. *Photosynth. Res.* **2010**, *104*, 245–255.
(16) Orf, G. S.; Blankenship, R. E. *Photosynth. Res.* **2013**, *116*, 315–331.
(17) Hohmann-Marriott, M. F.; Blankenship, R. E. *Annu. Rev. Plant Biol.* **2011**, *62*, 515–548.
(18) Maly, P.; Van Grondelle, R. *Curr. Opin. Chem. Biol.* **2018**, *47*, 1–6.
(19) Fassioli, F.; Dinshaw, R.; Arpin, P. C.; Scholes, G. D. *J. R. Soc. Interface* **2014**, *11*, 20130901.
(20) Chenu, A.; Scholes, G. D. *Annu. Rev. Phys. Chem.* **2015**, *66*, 69–96.
(21) Rebentrost, P.; Mohseni, M.; Kassal, I.; Lloyd, S.; Aspuru-Guzik, A. *New J. Phys.* **2009**, *11*, 033003.
(22) Ishizaki, A.; Fleming, G. R. *Proc. Natl. Acad. Sci. U. S. A.* **2009**, *106*, 17255–17260.
(23) Panitchayangkoon, G.; Hayes, D.; Fransted, K. A.; Caram, J. R.; Harel, E.; Wen, J.; Blankenship, R. E.; Engel, G. S. *Proc. Natl. Acad. Sci. U. S. A.* **2010**, *107*, 12766–12770.
(24) Duan, H.; Prokhorenko, V. I.; Cogdell, R. J.; Ashraf, K.; Stevens, A. L.; Thorwart, M.; Miller, R. J. D. *Proc. Natl. Acad. Sci. U. S. A.* **2017**, *114*, 8493–8498.
(25) Balaban, T. S. *Accounts Chem. Res.* **2005**, *38*, 612–623.
(26) Miyatake, T.; Tamiaki, H. *Coord. Chem. Rev.* **2010**, *254*, 2593–2602.
(27) Hiramoto, M.; Kitada, K.; Iketaki, K.; Kaji, T. *Appl. Phys. Lett.* **2011**, *98*, 023302.
(28) Eisele, D. M.; Cone, C. W.; Bloemsma, E. A.; Vlaming, S. M.; Van Der Kwaak, C. G. F.; Silbey, R. J.; Bawendi, M. G.; Knoester, J; Rabe, J. P.; Vanden Bout, D. A. *Nat. Chem.* **2012**, *4*, 655–662.

(29) Grosso, G.; Graves, J.; Hammack, A. T.; High, A. A.; Butov, L. V.; Hanson, M.; Gossard, A. C. *Nat. Photonics* **2009**, *3*, 577–580.
(30) Modesto-Lopez, L. B.; Thimsen, E. J.; Collins, A. M.; Blankenship, R. E.; Biswas, P. *Energy Environ. Sci.* **2010**, *3*, 216–222.
(31) Akselrod, G. M.; Walker, B. J.; Tisdale, W. A.; Bawendi, M. G.; Bulovic, V. *ACS Nano* **2012**, *6*, 467–471.
(32) Harmatys, K. M.; Chen, J.; Charron, D. M.; Maclaughlin, C. M.; Zheng, G. *Angew. Chem. Int. Edit.* **2018**, *57*, 8125–8129.
(33) De Groot, H. J. M., *Photosynthetic Antennae and Reaction Centers. In: eMagRes*; Harris, R., Wasylishen, R., Eds.; John Wiley & Sons, Ltd.: 2009.
(34) Adams, P. G.; Cadby, A. J.; Robinson, B.; Tsukatani, Y.; Tank, M.; Wen, J.; Blankenship, R. E.; Bryant, D. A.; Hunter, C. N. *Biochim. Biophys. Acta-Bioenerg.* **2013**, *1827*, 1235–1244.
(35) Tang, J.; Saikin, S.; Pingali, S.; Enriquez, M.; Huh, J; Frank, H.; Urban, V.; Aspuru-Guzik, A. *Biophys. J.* **2013**, *105*, 1346–1356.
(36) Linnanto, J. M.; Korppi-Tommola, J. E. L. *J. Phys. Chem. B* **2013**, *117*, 11144–11161.
(37) Ganapathy, S.; Oostergetel, G. T.; Wawrzyniak, P. K.; Reus, M.; Chew, A. G. M.; Buda, F.; Boekema, E. J.; Bryant, D. A.; Holzwarth, A. R.; De Groot, H. J. M. *Proc. Natl. Acad. Sci. U. S. A.* **2009**, *106*, 8525–8530.
(38) Oostergetel, G. T.; Reus, M.; Chew, A. G. M.; Bryant, D. A.; Boekema, E. J.; Holzwarth, A. R. *FEBS Lett.* **2007**, *581*, 5435–5439.
(39) Ganapathy, S.; Oostergetel, G. T.; Reus, M.; Tsukatani, Y.; Gomez Maqueo Chew, A.; Buda, F.; Bryant, D. A.; Holzwarth, A. R.; De Groot, H. J. M. *Biochemistry* **2012**, *51*, 4488–4498.
(40) Fujita, T.; Brookes, J. C.; Saikin, S. K.; Aspuru-Guzik, A. *J. Phys. Chem. Lett.* **2012**, *3*, 2357–2361.
(41) Huh, J.; Saikin, S. K.; Brookes, J. C.; Valleau, S.; Fujita, T.; Aspuru-Guzik, A. *J. Am. Chem. Soc.* **2014**, *136*, 2048–2057.
(42) Valleau, S.; Saikin, S. K.; Ansari-Oghol-beig, D.; Rostami, M.; Mossallaei, H.; Aspuru-Guzik, A. *ACS Nano* **2014**, *8*, 3884–3894.
(43) Fujita, T.; Huh, J.; Saikin, S. K.; Brookes, J. C.; Aspuru-Guzik, A. *Photosynth. Res.* **2014**, *120*, 273–289.
(44) Sawaya, N. P. D.; Huh, J.; Fujita, T.; Saikin, S. K.; Aspuru-Guzik, A. *Nano Lett.* **2015**, *15*, 1722–1729.
(45) Günther, L. M.; Jendrny, M.; Bloemsma, E. A.; Tank, M.; Oostergetel, G. T.; Bryant, D. A.; Knoester, J.; Köhler, J. *J. Phys. Chem. B* **2016**, *120*, 5367–5376.
(46) Günther, L. M.; Loehner, A.; Reiher, C.; Kunsel, T.; Jansen, T. L. C.; Tank, M.; Bryant, D. A.; Knoester, J.; Köhler, J. *J. Phys. Chem. B* **2018**, *122*, 6712–6723.
(47) Marrink, S. J.; Tieleman, D. P. *Chem. Soc. Rev.* **2013**, *42*, 6801–6822.
(48) Eisele, D. M.; Arias, D. H.; Fu, X.; Bloemsma, E. A.; Steiner, C. P.; Jensen, R. A.; Rebentrost, P.; Eisele, H.; Tokmakoff, A.; Lloyd, S.; Nelson, K. A.; Nicastro, D.; Knoester, J.; Bawendi, M. G. *Proc. Natl. Acad. Sci. U. S. A.* **2014**, *111*, E3367–E3375.
(49) Caram, J. R.; Doria, S.; Eisele, D. M.; Freyria, F. S.; Sinclair, T. S.; Rebentrost, P.; Lloyd, S.; Bawendi, M. G. *Nano Lett.* **2016**, *16*, 6808–6815.
(50) Cui, Q. H.; Peng, Q.; Luo, Y.; Jiang, Y.; Yan, Y.; Wei, C.; Shuai, Z.; Sun, C.; Yao, J.; Zhao, Y. S. *Sci. Adv.* **2018**, *4*, eaap9861.
(51) Frederix, P. W. J. M.; Patmanidis, I.; Marrink, S. J. *Chem. Soc. Rev.* **2018**, *47*, 3470–3489.
(52) Bryant, D. A.; Frigaard, N. *Trends Microbiol.* **2006**, *14*, 488–496.
(53) Blankenship, R. E., *Molecular mechanisms of photosynthesis*; John Wiley & Sons: 2014.
(54) Hall, D.; Coombs, J. In *Report No. 5, Energy from the biomass*; The Watt Committee on Energy Ltd: London, 1979, pp 2–15.

(55) Hanada, S.; Hiraishi, A.; Shimada, K.; Matsuura, K. *Int. J. Syst. Bacteriol.* **1995**, *45*, 676–681.
(56) Manske, A. K.; Glaeser, J.; Kuypers, M. A. M.; Overmann, J. *Appl. Environ. Microbiol.* **2005**, *71*, 8049–8060.
(57) Marschall, E.; Jogler, M.; Hessge, U.; Overmann, J. *Environ. Microbiol.* **2010**, *12*, 1348–1362.
(58) Bryant, D. A.; Costas, A. M. G.; Maresca, J. A.; Chew, A. G. M.; Klatt, C. G.; Bateson, M. M.; Tallon, L. J.; Hostetler, J.; Nelson, W. C.; Heidelberg, J. F.; Ward, D. M. *Science* **2007**, *317*, 523–526.
(59) Frigaard, N.; Voigt, G. D.; Bryant, D. A. *J. Bacteriol.* **2002**, *184*, 3368–3376.
(60) Frigaard, N.; Bryant, D. A. In *Complex Intracellular Structures in Prokaryotes*, Shively, J. M., Ed.; Springer Berlin Heidelberg: Berlin, Heidelberg, 2006, pp 79–114.
(61) Dostal, J.; Psencik, J.; Zigmantas, D. *Nat. Chem.* **2016**, *8*, 705–710.
(62) Coles, D.; Flatten, L. C.; Sydney, T.; Hounslow, E.; Saikin, S. K.; Aspuru-Guzik, A.; Vedral, V.; Tang, J. K.-H.; Taylor, R. A.; Smith, J. M.; Lidzey, D. G. *Small* **2017**, *13*.
(63) Sachse, C. *AIMS Biophysics* **2015**, *2*, 219–244.
(64) Ponder, J. W.; Case, D. A. In *Advances in Protein Chemistry*; Elsevier: 2003, pp 27–85.
(65) Hollingsworth, S. A.; Dror, R. O. *Neuron* **2018**, *99*, 1129–1143.
(66) Rapaport, D. C.; Rapaport, D. C. R., *The art of molecular dynamics simulation*; Cambridge university press: 2004.
(67) Alster, J.; Kabeláč, M.; Tuma, R.; Pšenčík, J.; Burda, J. *Comput. Theor. Chem.* **2012**, *998*, 87–97.
(68) Scholes, G. D.; Rumbles, G. *Nat. Mater.* **2006**, *5*, 683–696.
(69) Frenkel, J. *Phys. Rev.* **1931**, *37*, 17–44.
(70) Davydov, A. S. *Soviet Physics Uspekhi* **1964**, *7*, 145.
(71) Brixner, T.; Hildner, R.; Koehler, J.; Lambert, C.; Wuerthner, F. *Adv. Energy Mater.* **2017**, *7*, 1700236.
(72) Adolphs, J.; Müh, F.; Madjet, M.; Renger, T. *Photosynth. Res.* **2008**, *95*, 197–209.
(73) González, L.; Escudero, D.; Serrano-Andrés, L. *ChemPhysChem* **2012**, *13*, 28–51.
(74) Rivera, E.; Montemayor, D.; Masia, M.; Coker, D. F. *J. Phys. Chem. B* **2013**, *117*, 5510–5521.
(75) Cupellini, L.; Jurinovich, S.; Campetella, M.; Caprasecca, S.; Guido, C. A.; Kelly, S. M.; Gardiner, A. T.; Cogdell, R.; Mennucci, B. *J. Phys. Chem. B* **2016**, *120*, 11348–11359.
(76) Kenny, E. P.; Kassal, I. *J. Phys. Chem. B* **2016**, *120*, 25–32.
(77) Curutchet, C.; Mennucci, B. *Chem. Rev.* **2017**, *117*, 294–343.
(78) Pearlstein, R. M. In *Chlorophylls*, Scheer, H., Ed.; CRC Press: Boca Raton, 1991, pp 1047–1078.
(79) Didraga, C.; Klugkist, J. A.; Knoester, J. *J. Phys. Chem. B* **2002**, *106*, 11474–11486.
(80) Prokhorenko, V. I.; Steensgaard, D. B.; Holzwarth, A. R. *Biophys. J.* **2003**, *85*, 3173–3186.
(81) Susskind, L., *Quantum Mechanics: The Theoretical Minimum*; Basic Books: 2014.
(82) Monti, A.; Negre, C. F. A.; Batista, V. S.; Rego, L. G. C.; De Groot, H. J. M.; Buda, F. *J. Phys. Chem. Lett.* **2015**, *6*, 2393–2398.
(83) Shi, L.; Willard, A. P. *J. Chem. Phys.* **2018**, *149*, 094110.
(84) Dostal, J.; Mancal, T.; Vacha, F.; Psencik, J.; Zigmantas, D. *J. Chem. Phys.* **2014**, *140*, 115103.
(85) Caruso, F.; Chin, A. W.; Datta, A.; Huelga, S. F.; Plenio, M. B. *J. Chem. Phys.* **2009**, *131*, 105106.
(86) Tian, Y.; Camacho, R.; Thomsson, D.; Reus, M.; Holzwarth, A. R.; Scheblykin, I. G. *J. Am. Chem. Soc.* **2011**, *133*, 17192–17199.

(87) Van Amerongen, H.; Van Haeringen, B.; Van Gurp, M.; Van Grondelle, R. *Biophys. J.* **1991**, *59*, 992–1001.
(88) Griebenow, K; Holzwarth, A.; Vanmourik, F; Vangrondelle, R **1991**, *1058*, 194–202.
(89) Marques, H.; Brown, K. *Coord. Chem. Rev.* **2002**, *225*, 123–158.
(90) Ansari-Oghol-beig, D.; Rostami, M.; Chernobrovkina, E.; Saikin, S. K.; Valleau, S.; Mosallaei, H.; Aspuru-Guzik, A. *J. Appl. Phys.* **2013**, *114*, 164315.
(91) Jorgensen, W. L.; Maxwell, D. S.; Tiradorives, J. *J. Am. Chem. Soc.* **1996**, *118*, 11225–11236.
(92) Kaminski, G. A.; Friesner, R. A.; Tirado-Rives, J; Jorgensen, W. L. *J. Phys. Chem. B* **2001**, *105*, 6474–6487.
(93) Karki, K.; Roccatano, D. *J. Chem. Theory Comput.* **2011**, *7*, 1131–1140.
(94) Cornell, W. D.; Cieplak, P; Bayly, C. I.; Kollman, P. A. *J. Am. Chem. Soc.* **1993**, *115*, 9620–9631.
(95) Frish, M.; Trucks, G.; Schlegel, H.; Scuseria, G.; Robb, M.; Cheeseman, J.; Zakrzevski, V.; Montgomery Jr, J.; Vreven, T; Kudin, K.; Others *Gaussian 03, Revision D. 03, Gaussian, Inc., Wallingford CT,* **2004**.
(96) Hess, B.; Kutzner, C.; Van Der Spoel, D.; Lindahl, E. *J. Chem. Theory Comput.* **2008**, *4*, 435–447.
(97) Abraham, M. J.; Murtola, T.; Schulz, R.; Páll, S.; Smith, J. C.; Hess, B.; Lindahl, E. *SoftwareX* **2015**, *1-2*, 19–25.
(98) Essmann, U.; Perera, L.; Berkowitz, M. L.; Darden, T.; Lee, H.; Pedersen, L. G. *J. Chem. Phys.* **1995**, *103*, 8577–8593.
(99) Bussi, G.; Donadio, D.; Parrinello, M. *J. Chem. Phys.* **2007**, *126*, 014101.
(100) Balaban, T. S.; Leitich, J.; Holzwarth, A. R.; Schaffner, K. *J. Phys. Chem. B* **2000**, *104*, 1362–1372.
(101) Coudray, N.; Lasala, R.; Zhang, Z.; Clark, K. M.; Dumont, M. E.; Stokes, D. L. *J. Struct. Biol.* **2016**, *195*, 167–178.
(102) Orgel, J. P.; Persikov, A. V.; Antipova, O. *PLoS One* **2014**, *9*, e89519.
(103) Amos, L. A.; Hirose, K. *Methods Mol. Med.* **2007**, *137*, 65–91.
(104) Furumaki, S.; Vacha, F.; Habuchi, S.; Tsukatani, Y.; Bryant, D. A.; Vacha, M. *J. Am. Chem. Soc.* **2011**, *133*, 6703–6710.
(105) Marquez, A. S.; Chen, L.; Sun, K.; Zhao, Y. *Phys. Chem. Chem. Phys.* **2016**, *18*, 20298–20311.
(106) Moody, M. F. In *Structural biology using electrons and X-rays: an introduction for biologists*; Academic Press: Boston, 2011, pp 311–335.
(107) Van Amerongen, H.; Vasmel, H.; Van Grondelle, R. *Biophys. J.* **1988**, *54*, 65–76.
(108) Balaban, T. S.; Holzwarth, A. R.; Schaffner, K.; Boender, G.; De Groot, H. J. M. *Biochemistry* **1995**, *34*, 15259–15266.
(109) Connolly, M. *Science* **1983**, *221*, 709–713.
(110) Chow, H.; Serlin, R.; Strouse, C. E. *J. Am. Chem. Soc.* **1975**, *97*, 7230–7237.
(111) Umetsu, M.; Wang, Z.; Zhang, J.; Ishii, T.; Uehara, K.; Inoko, Y.; Kobayashi, M.; Nozawa, T. *Photosynth. Res.* **1999**, *60*, 229–239.
(112) Pandit, A.; Ocakoglu, K.; Buda, F.; Van Marle, T.; Holzwarth, A. R.; De Groot, H. J. M. *J. Phys. Chem. B* **2013**, *117*, 11292–11298.
(113) Garab, G.; Van Amerongen, H. *Photosynth. Res.* **2009**, *101*, 135–146.
(114) Kim, M.; Ulibarri, L.; Keller, D.; Maestre, M. F.; Bustamante, C. *J. Chem. Phys.* **1986**, *84*, 2981–2989.
(115) Furumaki, S.; Yabiku, Y.; Habuchi, S.; Tsukatani, Y.; Bryant, D. A.; Vacha, M. *J. Phys. Chem. Lett.* **2012**, *3*, 3545–3549.

(116) Blankenship, R. E.; Olson, J. M.; Miller, M. In *Anoxygenic Photosynthetic Bacteria*, Blankenship, R. E., Madigan, M. T., Bauer, C. E., Eds.; Springer Netherlands: Dordrecht, 1995, pp 399–435.
(117) Blankenship, R. E.; Matsuura, K. In *Light-Harvesting Antennas in Photosynthesis*, Green, B. R., Parson, W. W., Eds.; Springer Netherlands: Dordrecht, 2003, pp 195–217.
(118) Ganapathy, S.; Sengupta, S.; Wawrzyniak, P. K.; Huber, V.; Buda, F.; Baumeister, U.; Wuerthner, F.; De Groot, H. J. M. *Proc. Natl. Acad. Sci. U. S. A.* **2009**, *106*, 11472–11477.
(119) Saikin, S. K.; Eisfeld, A.; Valleau, S.; Aspuru-Guzik, A. *Nanophotonics* **2013**, *2*, 21–38.
(120) Dostál, J.; Mančal, T.; Augulis, R.; Vácha, F.; Pšenčík, J.; Zigmantas, D. *J. Am. Chem. Soc.* **2012**, *134*, 11611–11617.
(121) Jun, S.; Yang, C.; Kim, T. W.; Isaji, M.; Tamiaki, H.; Ihee, H.; Kim, J. *Phys. Chem. Chem. Phys.* **2015**, *17*, 17872–17879.
(122) Agranovich, V. M.; Galanin, M. D., *Electronic Excitation Energy Transfer in Condensed Matter*; North-Holland: 1982; Vol. 3.
(123) Oviedo, M. B.; Sánchez, C. G. *J. Phys. Chem. A* **2011**, *115*, 12280–12285.
(124) Prokhorenko, V. I.; Steensgaard, D. B.; Holzwarth, A. R. *Biophys. J.* **2000**, *79*, 2105–2120.
(125) Kriete, B.; Bondarenko, A. S.; Jumde, V. R.; Franken, L. E.; Minnaard, A. J.; Jansen, T. L. C.; Knoester, J.; Pshenichnikov, M. S. *J. Phys. Chem. Lett.* **2017**, *8*, 2895–2901.
(126) Bloemsma, E. A.; Vlaming, S. M.; Malyshev, V. A.; Knoester, J. *Phys. Rev. Lett.* **2015**, *114*, 156804.
(127) Molina, R. A.; Benito-Matías, E.; Somoza, A. D.; Chen, L.; Zhao, Y. *Phys. Rev. E* **2016**, *93*, 022414.
(128) Rancova, O.; Abramavicius, D. *J. Phys. Chem. B* **2014**, *118*, 7533–7540.
(129) Matysik, J.; Alia; Gast, P.; Van Gorkom, H. J.; Hoff, A. J.; De Groot, H. J. M. *Proc. Natl. Acad. Sci. U. S. A.* **2000**, *97*, 9865–9870.
(130) Caffarri, S.; Tibiletti, T.; Jennings, R. C.; Santabarbara, S. *Curr. Protein Pept. Sci.* **2014**, *15*, 296–331.
(131) Bouvier, B.; Dognon, J.; Lavery, R.; Markovitsi, D.; Millie, P.; Onidas, D.; Zakrzewska, K. *J. Phys. Chem. B* **2003**, *107*, 13512–13522.
(132) Van Dorssen, R. J.; Vasmel, H.; Amesz, J. *Photosynth. Res.* **1986**, *9*, 33–45.
(133) Griebenow, K.; Holzwarth, A. R. *Biochim. Biophys. Acta* **1989**, *973*, 235–240.
(134) Lehmann, R. P.; Brunisholz, R. A.; Zuber, H. *Photosynth. Res.* **1994**, *41*, 165–173.
(135) Frese, R.; Oberheide, U.; Van Stokkum, I.; Van Grondelle, R.; Foidl, M.; Oelze, J.; Van Amerongen, H. *Photosynth. Res.* **1997**, *54*, 115–126.
(136) Tang, K.; Zhu, L; Urban, V.; Collins, A.; Biswas, P; Blankenship, R. *Langmuir* **2011**, *27*, 4816–4828.
(137) Betti, J. A.; Blankenship, R. E.; Natarajan, L. V.; Dickinson, L. C.; Fuller, R. C. *Biochim. Biophys. Acta, Bioenerg.* **1982**, *680*, 194–201.
(138) Eisfeld, A.; Briggs, J. *Chem. Phys.* **2006**, *324*, 376–384.
(139) Even, J.; Carignano, M.; Katan, C. *Nanoscale* **2016**, *8*, 6222–6236.
(140) Jang, S. J.; Mennucci, B. *Rev. Mod. Phys.* **2018**, *90*, 035003.
(141) Jun, S.; Yang, C.; Isaji, M.; Tamiaki, H.; Kim, J.; Ihee, H. *J. Phys. Chem. Lett.* **2014**, *5*, 1386–1392.
(142) Rathbone, H. W.; Davis, J. A.; Michie, K. A.; Goodchild, S. C.; Robertson, N. O.; Curmi, P. M. G. *Biophys. Rev.* **2018**, *10*, 1443–1463.
(143) Alia, A.; Buda, F.; De Groot, H. J. M.; Matysik, J. *Annu. Rev. Biophys.* **2013**, *42*, 675–699.
(144) Dama, J. F.; Sinitskiy, A. V.; Mccullagh, M.; Weare, J.; Roux, B.; Dinner, A. R.; Voth, G. A. *J. Chem. Theory Comput.* **2013**, *9*, 2466–2480.

(145) Tapavicza, E.; Bellchambers, G. D.; Vincent, J. C.; Furche, F. *Phys. Chem. Chem. Phys.* **2013**, *15*, 18336.
(146) Psencik, J.; Polivka, T.; Nemec, P.; Dian, J.; Kudrna, J.; Maly, P.; Hala, J. *J. Phys. Chem. A* **1998**, *102*, 4392–4398.
(147) Martiskainen, J.; Linnanto, J.; Aumanen, V.; Myllyperkio, P.; Korppi-Tommola, J. *Photochem. Photobiol.* **2012**, *88*, 675–683.
(148) Renger, T. *Photosynth. Res.* **2009**, *102*, 471–485.
(149) Chenu, A.; Maly, P.; Mancal, T. *Chem. Phys.* **2014**, *439*, 100–110.
(150) Brown, P. N.; Byrne, G. D.; Hindmarsh, A. C. *SIAM J. Sci. Comput.* **1989**, *10*, 1038–1051.
(151) Johansson, J. R.; Nation, P. D.; Nori, F. *Comput. Phys. Commun.* **2013**, *184*, 1234–1240.
(152) Fassioli, F.; Olaya-Castro, A.; Scholes, G. D. *J. Phys. Chem. Lett.* **2012**, *3*, 3136–3142.
(153) Haken, H.; Reineker, P. *Z. Physik* **1972**, *249*, 253–268.
(154) Haken, H.; Strobl, G. *Z. Physik* **1973**, *262*, 135–148.
(155) Huijser, A.; Savenije, T. J.; Meskers, S. C. J.; Vermeulen, M. J. W.; Siebbeles, L. D. A. *J. Am. Chem. Soc.* **2008**, *130*, 12496–12500.
(156) Tempelaar, R.; Jansen, T. L. C.; Knoester, J. *J. Phys. Chem. B* **2014**, *118*, 12865–12872.
(157) Staehelin, L. A.; Golecki, J. R.; Drews, G. *Biochim. Biophys. Acta* **1980**, *589*, 30–45.
(158) Bondarenko, A. S.; Knoester, J.; Jansen, T. L. C. *Chem. Phys.* **2020**, *529*, 110478.
(159) Pauling, L.; Corey, R. B.; Branson, H. R. *Proc. Natl. Acad. Sci. U. S. A.* **1951**, *37*, 205–211.
(160) Watson, J.; Crick, F. *Nature* **1953**, *171*, 737–738.
(161) Dauter, Z.; Jaskolski, M. *Protein Sci.* **2018**, *27*, 643–652.
(162) Wagstaff, J.; Lowe, J. *Nat. Rev. Microbiol.* **2018**, *16*, 187–201.
(163) Craig, R; Woodhead, J. *Curr. Opin. Struct. Biol.* **2006**, *16*, 204–212.
(164) Imada, K. *Biophys. Rev.* **2018**, *10*, 559–570.
(165) Rakonjac, J.; Bennett, N. J.; Spagnuolo, J.; Gagic, D.; Russel, M. *Curr. Issues Mol. Biol.* **2011**, *13*, 51–75.
(166) Snir, Y.; Kamien, R. D. *Science* **2005**, *307*, 1067–1067.
(167) Solis, F. J.; Vernizzi, G.; De La Cruz, M. O. *Soft Matter* **2011**, *7*, 1456–1466.
(168) Aida, T.; Meijer, E. W.; Stupp, S. I. *Science* **2012**, *335*, 813–817.
(169) Sengupta, S.; Würthner, F. *Acc. Chem. Res.* **2013**, *46*, 2498–2512.
(170) Liu, M.; Zhang, L.; Wang, T. *Chem. Rev.* **2015**, *115*, 7304–7397.
(171) Yashima, E.; Ousaka, N.; Taura, D.; Shimomura, K.; Ikai, T.; Maeda, K. *Chem. Rev.* **2016**, *116*, 13752–13990.
(172) Didraga, C.; Pugžlys, A.; Hania, P. R.; Von Berlepsch, H.; Duppen, K.; Knoester, J. *J. Phys. Chem. B* **2004**, *108*, 14976–14985.
(173) Jin, W.; Fukushima, T.; Niki, M.; Kosaka, A.; Ishii, N.; Aida, T. *Proc. Natl. Acad. Sci. U. S. A.* **2005**, *102*, 10801–10806.
(174) Short, J. M.; Berriman, J. A.; Kübel, C.; El-Hachemi, Z.; Naubron, J.; Balaban, T. S. *ChemPhysChem* **2013**, *14*, 3209–3214.
(175) Wan, Y.; Stradomska, A.; Fong, S.; Guo, Z.; Schaller, R. D.; Wiederrecht, G. P.; Knoester, J.; Huang, L. *J. Phys. Chem. C* **2014**, *118*, 24854–24865.
(176) Prokhorov, V. V.; Perelygina, O. M.; Pozin, S. I.; Mal'tsev, E. I.; Vannikov, A. V. *J. Phys. Chem. B* **2015**, *119*, 15046–15053.
(177) Friedl, C.; Renger, T.; Berlepsch, H. V.; Ludwig, K.; Schmidt Am Busch, M.; Megow, J. *J. Phys. Chem. C* **2016**, *120*, 19416–19433.
(178) Pandya, R.; Chen, R. Y. S.; Cheminal, A.; Thomas, T.; Thampi, A.; Tanoh, A.; Richter, J.; Shivanna, R.; Deschler, F.; Schnedermann, C.; Rao, A. *J. Phys. Chem. Lett.* **2018**, *9*, 5604–5611.

(179) Doria, S.; Sinclair, T. S.; Klein, N. D.; Bennett, D. I. G.; Chuang, C.; Freyria, F. S.; Steiner, C. P.; Foggi, P.; Nelson, K. A.; Cao, J.; Aspuru-Guzik, A.; Lloyd, S.; Caram, J. R.; Bawendi, M. G. *ACS Nano* **2018**, *12*, 4556–4564.
(180) Matsubara, S.; Tamiaki, H. *J. Am. Chem. Soc.* **2019**, *141*, 1207–1211.
(181) Haedler, A. T.; Kreger, K.; Issac, A.; Wittmann, B.; Kivala, M.; Hammer, N.; Köhler, J.; Schmidt, H. W.; Hildner, R. *Nature* **2015**, *523*, 196–199.
(182) Qin, F.; Shi, W.; Ideue, T.; Yoshida, M.; Zak, A.; Tenne, R.; Kikitsu, T.; Inoue, D.; Hashizume, D.; Iwasa, Y. *Nat. Commun.* **2017**, *8*, 14465.
(183) Tsai, C.; Nussinov, R. *Acta Crystallogr., Sect. D: Biol. Crystallogr.* **2011**, *67*, 716–728.
(184) He, S.; Scheres, S. H. W. *J. Struct. Biol.* **2017**, *198*, 163–176.
(185) Damnjanovic, M.; Nikolic, B.; Milosevic, I. *Phys. Rev. B* **2007**, *75*, 033403.
(186) Qin, L. *Phys. Chem. Chem. Phys.* **2007**, *9*, 31–48.
(187) Huber, V.; Sengupta, S.; Wuerthner, F. *Chem. - Eur. J.* **2008**, *14*, 7791–7807.
(188) Ogi, S.; Grzeszkiewicz, C.; Wuerthner, F. *Chem. Sci.* **2018**, *9*, 2768–2773.
(189) Saunders, M. G.; Voth, G. A. *Annual Review of Biophysics* **2013**, *42*, 73–93.
(190) Ingólfsson, H. I.; Lopez, C. A.; Uusitalo, J. J.; De Jong, D. H.; Gopal, S. M.; Periole, X.; Marrink, S. J. *WIREs Computational Molecular Science* **2014**, *4*, 225–248.
(191) De Jong, D. H.; Liguori, N.; Van Den Berg, T.; Arnarez, C.; Periole, X.; Marrink, S. J. *J. Phys. Chem. B* **2015**, *119*, 7791–7803.
(192) Debnath, A.; Wiegand, S.; Paulsen, H.; Kremer, K.; Peter, C. *Phys. Chem. Chem. Phys.* **2015**, *17*, 22054–22063.
(193) Gemuenden, P.; Poelking, C.; Kremer, K.; Andrienko, D.; Daoulas, K. C. *Macromolecules* **2013**, *46*, 5762–5774.
(194) Gemuenden, P.; Poelking, C.; Kremer, K.; Daoulas, K.; Andrienko, D. *Macromol. Rapid Commun.* **2015**, *36*, 1047–1053.
(195) Meyers, M. A.; Chen, P.; Lin, A. Y.; Seki, Y. *Prog. Mater. Sci.* **2008**, *53*, 1–206.
(196) Parrinello, M.; Rahman, A. *J. Chem. Phys.* **1982**, *76*, 2662–2666.
(197) Mary, P.; Yamini, D.; Garegin, A. P., *Minimal Cylinder Analysis Reveals the Mechanical Properties of Oncogenic Nucleosomes*, 2019.
(198) Sotomayor, M.; Corey, D. P.; Schulten, K. *Structure* **2005**, *13*, 669–682.
(199) Buehler, M. J.; Wong, S. Y. *Biophys. J.* **2007**, *93*, 37–43.
(200) Luan, B.; Aksimentiev, A. *Phys. Rev. Lett.* **2008**, *101*, 118101.
(201) Zeiger, A. S.; Layton, B. E. *Biophys. J.* **2008**, *95*, 3606–3618.
(202) Wells, D. B.; Aksimentiev, A. *Biophys. J.* **2010**, *99*, 629–637.
(203) Kononova, O.; Kholodov, Y.; Theisen, K. E.; Marx, K. A.; Dima, R. I.; Ataullakhanov, F. I.; Grishchuk, E. L.; Barsegov, V. *J. Am. Chem. Soc.* **2014**, *136*, 17036–17045.
(204) Varma, S.; Orgel, J. P. R. O.; Schieber, J. D. *Biophys. J.* **2016**, *111*, 50–56.
(205) Nazarychev, V. M.; Lyulin, A. V.; Larin, S. V.; Gurtovenko, A. A.; Kenny, J. M.; Lyulin, S. V. *Soft Matter* **2016**, *12*, 3972–3981.
(206) Bringa, M.; Rosolankova, K.; Rudd, R. E.; Remington, B. A.; Wark, J. S.; Duchaineau, M.; Kalantar, H.; Hawreliak, J.; Belak, J. *Nat. Mater.* **2006**, *5*, 805–809.
(207) Zukas, J. A. In *Introduction to Hydrocodes*, Zukas, J. A., Ed.; Elsevier: 2004, pp 75–102.
(208) Holian, B. L. *Shock Waves* **1995**, *5*, 149–157.
(209) Gray, G. T. In *High-Pressure Shock Compression of Solids*, Asay, J. R., Shahinpoor, M., Eds.; Springer New York: New York, NY, 1993, pp 187–215.
(210) Holian, B.; Lomdahl, P. *Science* **1998**, *280*, 2085–2088.
(211) Germann, T. C.; Holian, B. L.; Lomdahl, P. S.; Ravelo, R. *Phys. Rev. Lett.* **2000**, *84*, 5351–5354.
(212) Lau, E. Y.; Berkowitz, M. L.; Schwegler, E. *Biophys. J.* **2016**, *110*, 147–156.
(213) Froehlich, M. G.; Sewell, T. D.; Thompson, D. L. *J. Chem. Phys.* **2014**, *140*, 024902.

(214) Fu, Y.; Michopoulos, J.; Song, J. *J. Polym. Sci. Pt. B-Polym. Phys.* **2015**, *53*, 1292–1302.
(215) Xie, F.; Lu, Z.; Yang, Z.; Hu, W.; Yuan, Z. *Polymer* **2016**, *98*, 294–304.
(216) O'connor, T. C.; Elder, R. M.; Sliozberg, Y. R.; Sirk, T. W.; Andzelm, J. W.; Robbins, M. O. *Phys. Rev. Mater.* **2018**, *2*, 035601.
(217) An, Q.; Cheng, T.; Goddard William A, I.; Zybin, S. V. *J. Phys. Chem. C* **2015**, *119*, 2196–2207.
(218) Kfoury, R.; Marzban, B.; Makki, E.; Greenfield, M. L.; Yuan, H. *PLoS One* **2019**, *14*, e0212566.
(219) Li, B.; Li, X.; Chen, M. *Phys. Fluids* **2017**, *29*, 012003.
(220) Wu, Y.; Adnan, A. *Sci. Rep.* **2018**, *8*, 12260.
(221) Schaedel, L.; John, K.; Gaillard, J.; Nachury, M. V.; Blanchoin, L.; Thery, M. *Nat. Mater.* **2015**, *14*, 1156–1163.
(222) Berendsen, H. J. C. In *Computational Molecular Dynamics: Challenges, Methods, Ideas*, Deuflhard, P., Hermans, J., Leimkuhler, B., Mark, A. E., Reich, S., Skeel, R. D., Eds.; Springer Berlin Heidelberg: Berlin, Heidelberg, 1999, pp 3–36.
(223) Ishil, T.; Kimura, M.; Yamamoto, T.; Kirihata, M.; Uehara, K. *Photochem. Photobiol.* **2000**, *71*, 567–573.
(224) Sørensen, P. G.; Cox, R. P.; Miller, M. *Photosynth. Res.* **2008**, *95*, 191–196.
(225) Saga, Y.; Akai, S.; Miyatake, T.; Tamiaki, H. *Bioconjug. Chem.* **2006**, *17*, 988–994.
(226) Berendsen, H.; Postma, J.; Vangunsteren, W.; Dinola, A; Haak, J. *J. Chem. Phys.* **1984**, *81*, 3684–3690.
(227) Parrinello, M.; Rahman, A. *J. Appl. Phys.* **1981**, *52*, 7182–7190.
(228) Nosé, S.; Klein, M. L. *Mol. Phys.* **1983**, *50*, 1055–1076.
(229) Car, R.; Parrinello, M. *Phys. Rev. Lett.* **1985**, *55*, 2471–2474.
(230) Lin, I.; Coutinho-Neto, M. D.; Felsenheimer, C.; Von Lilienfeld, O. A.; Tavernelli, I.; Rothlisberger, U. *Phys. Rev. B* **2007**, *75*, 205131.
(231) Nosé, S. *J. Chem. Phys.* **1984**, *81*, 511–519.
(232) Hoover, W. G. *Phys. Rev. A* **1985**, *31*, 1695–1697.
(233) Pedregosa, F. et al. *J. Mach. Learn. Res.* **2011**, *12*, 2825–2830.